Numerical study of the temperature-dependent magnetization and susceptibility of Tm³⁺ in LiTmF₄

Leila Mollabashi [1], S. Jalali-Asadabadi [1,*], Czesław Rudowicz [2], Muhammed Acikgoz [3], Zahra Ghasemi-Dorcheh [1],
Reyhaneh Ebrahimi-Jaberi [1], Mahdi Jalali-Asadabadi [1], Shahrbano Rahimi [1], and Farhad Jalali-Asadabadi [1,4]

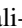[1]*Department of Physics, Faculty of Physics, University of Isfahan (UI), Hezar Jerib Avenue, Isfahan 81746-73441, Iran*
[2]*Faculty of Chemistry, A. Mickiewicz University (AMU), 61-614 Poznań, Poland*
[3]*Department of Science, The State University of New York (SUNY) Maritime College, New York 10465, USA*
[4]*Physics Department, Faculty of Science, Razi University, Taq-e Bostan, Kermanshah 6714414971, Iran*

Studying magnetic properties of LiTmF₄, a recognized insulating Van Vleck paramagnet, can hold promise for advancements in quantum computing, MRI, spintronics, material design, and potentially, single-photon technologies. This study may be pivotal due to challenges in simulating noncollinear magnetism using density functional theory (DFT), requiring more sophisticated spin configurations and time-consuming spin relaxations or embedded dynamical mean field theory. Instead, we utilize two distinct efficient and reliable schemes—*ab initio* DFT and a semiempirical superposition model, both integrated with crystal field (CF) theory (including Zeeman effect) and underpinned by statistical mechanics—to analyze noncollinear paramagnetic properties. At the core of this investigation is the S_4 site symmetry of the Tm³⁺ ion, which admits several sets of six (seven) independent CF parameters (CFPs) under the reduced (complete) approach generated by suitable rotations of the coordinate system. By applying the Noether theorem, we show that these numerically distinct sets are physically equivalent. This is evidenced by computing the several conserved CFP quantities predicted by the Noether theorem, which exhibit notable coherence across different data sets. Using one of these equivalent sets of 7 CF parameters, as computed in [Phys. Rev. B **102**, 045120 (2020)] under the complete approach, this study explores the theoretical analysis of multiplet splitting induced by the CF and the external magnetic field within the Tm³⁺ ion lattice in LiTmF₄. We investigate the magnetic moment per ion and the temperature dependencies of magnetic susceptibility, utilizing a Hamiltonian, including the free ion, CF terms, and Zeeman interaction. The agreement of our findings with existing experimental data accentuates the efficacy of the proposed approach in reproducing magnetic properties in LiTmF₄, providing a significant analytical tool for the analysis of EPR spectra in terms of the defined Zeeman **g** tensor. This research may stand as a pivotal guide in the accurate determination of magnetic properties, potentially influencing significant advancements in technology and materials science.

I. INTRODUCTION

LiRF₄ (R = rare earth) and LiYF₄:R³⁺ insulators are highly valued in industrial and quantum theoretical fields, renowned for their unique optical, electronic, and magnetic properties [1–8]. Their potential applications span quantum computing [9], MRI technology [10], spintronics [11], material design, and single-photon technology [12]. Rare-earth ions in solid-state hosts, like those in LiYF₄:R³⁺, are promising for quantum light sources [13] and laser applications [14]. The magnetic behaviors of LiRF₄ compounds, particularly LiTmF₄ known for its Van Vleck paramagnetism [15–17], vary across the rare-earth series, especially at low temperatures [8,14,18–23]. These compounds have been extensively studied through experimental and theoretical approaches, including quantum mechanical *ab initio* methods.

The magnetic properties of a material, particularly influenced by the crystal field (CF) interaction, play a crucial role in determining its ground state properties [24]. To accurately understand these properties, an in-depth knowledge of the CF interaction is essential. Despite its significance, density functional theory (DFT) studies on LiTmF₄ are comparatively limited, largely due to the complexities involved in simulating paramagnetic materials. In *ab initio* studies of such materials, a prevalent approach involves constructing a noncollinear magnetic structure with initially arbitrary spin angles, as detailed in the "Calculation details" and "Paramagnetic phase" sections of Ref. [25]. This structure undergoes a relaxation process, leading to the final magnetic configuration within the unit cell. The spatial relaxation of spins, however, introduces significant computational challenges, escalating the overall computational cost [25]. Overcoming these challenges typically necessitates time-intensive methods such as the noncollinear magnetism approach in the WIENNCM code [26], and the DFT + DMFT method in the embedded dynamical mean field theory (eDMFT) code [27]. The WIENNCM code [26], a noncollinear version of the WIEN2K code [28], enables the treatment of arbitrary noncollinear spin structures (with spin-orbit coupling) and spin-spirals with arbitrary **q** vectors (without spin-orbit coupling). According to our recent

*Contact author: saeid.jalali.asadabadi@gmail.com; sjalali@sci.ui.ac.ir

experience [25], using this code presents a greater challenge compared to the standard WIEN2K code. Our recent experience [25] indicates that performing these noncollinear magnetism calculations is a sophisticated and labor-intensive process. Therefore, in this work, we introduce and implement two novel approaches aimed at enhancing the efficiency of such calculations.

To overcome the computational challenges inherent in simulating paramagnetic properties, as outlined above, we employ two distinct approaches: *ab initio* DFT and the semiempirical superposition model (SPM). These methods are first integrated with CF theory (CFT) and then further augmented with the principles of statistical mechanics. This advanced combination of DFT + CFT + Δ and SPM + CFT has proved effective in our recent study, where we successfully investigated the spectroscopic and magnetic properties of Gd^{3+}-doped $PbTiO_3$ [29]. Our current aim is to refine these approaches by incorporating statistical mechanics within its canonical ensemble framework. This enhancement is specifically designed to more accurately simulate the paramagnetic phase of compounds like $LiTmF_4$, particularly under moderate external magnetic fields. It allows for an in-depth exploration of their temperature-dependent magnetic properties. Moreover, the computational cost of our chosen methods, which focus on paramagnetic order, is roughly equivalent to a standard DFT calculation. This represents a significant reduction in computational demands compared to both WIENNCM and DFT + eDMFT approaches.

To understand the magnetic properties of $LiTmF_4$ and $LiYF_4$:Tm, it is crucial to analyze their CF parameters (CFPs) within the context of their shared scheelite structure, crystallizing in space group $C4h^6(I4_1/a)$ [30]. Both compounds feature two Tm^{3+} ions per unit cell with S_4 site symmetry, essential for determining CFPs. While previous studies, such as Klimin *et al.*'s [31], have identified seven CFPs in S_4 symmetry, challenges exist in determining all CFPs solely from optical spectra [32–35]. To address this, we adopt the R-(reduced) approach [32–34], nullifying one CFP to achieve a unique set of six CFPs, providing a more reliable framework for studying these compounds' magnetic properties. This streamlined approach enhances our understanding of their magnetic behavior within the scheelite structure, ensuring the accuracy and consistency of our findings.

Here, we accurately characterize the magnetic properties of Tm^{3+} ions in $LiTmF_4$, with a special focus on determining CFPs and understanding their impact on magnetic behavior. To this end, by applying the Noether theorem [34] in conjunction with CFT, we compute conserved quantities (CQs) and analyze various datasets to demonstrate that different CFPs sets, despite their numerical distinctions, are physically equivalent. While the complexity of S_4 symmetry can be bypassed using an approximate D_{2d} symmetry (A-approach), which requires only five real independent CFPs [36], our goal is a comprehensive analysis. This is exemplified by studies such as Jensen *et al.*'s work on energy levels and magnetic *g* tensor in $LiYF_4$:Tm^{3+} [37], and Kumar *et al.*'s research on Schottky specific heat and paramagnetic susceptibility in Tm^{3+}:$LiYF_4$ [38]. We recently employed an *ab initio* approach to determine all seven independent CFPs [36], providing a deeper insight into the temperature dependencies of magnetization and sus-

ceptibility for Tm^{3+} ions at S_4 symmetry sites in $LiTmF_4$. In this work, by combining the Noether theorem with our *ab initio* approach, we have effectively utilized continuous site symmetry principles for a thorough understanding of Tm^{3+} ions in $LiTmF_4$, achieving our goal of elucidating their behavior under various temperature conditions and highlighting the Noether theorem's critical role in our analysis.

Our research aims to deepen the understanding of $LiTmF_4$'s magnetic properties across different conditions, building upon foundational studies. Klochkov *et al.* explored the field and temperature dependencies of magnetization in $LiTmF_4$ powders within a range of 2–300 K and 0.0–5.5 T [39]. Abubakirov *et al.* extended this by measuring magnetization in $LiTmF_4$ single crystals from 2 to 300 K and 0 to 55 kOe, interpreting their findings through Christensen *et al.*'s C-approach [16,35]. Babkevich *et al.* contributed with inelastic neutron scattering measurements on $LiRF_4$ compounds, including Tm^{3+}, to study R^{3+} ions' transition energies [17]. By synthesizing these studies, our work integrates and contextualizes these findings to provide a more comprehensive understanding of $LiTmF_4$'s magnetic behavior under various experimental conditions, thus offering a clearer and more complete picture of its properties across a broad spectrum of temperature and magnetic field conditions.

In our study, we employ DFT + CFT + Δ and SPM + CFT methods, both enhanced with statistical mechanics, to investigate the magnetic properties of $LiTmF_4$, particularly its response to external magnetic fields. Using CF parameters from *ab initio* computations [36], we construct and diagonalize a Hamiltonian that includes the CF Hamiltonian $\hat{H}_{CF}$ and the effective Zeeman interaction. This allows us to calculate magnetic moments, Zeeman *g* tensor, and Van Vleck susceptibility tensor components for each eigenstate, and to compute temperature-dependent magnetization using Boltzmann statistics. A key aspect of our research is examining the splittings of the excited $\Gamma_{3,4}^1(^3H_6)$ doublet states under an external magnetic field up to 1 T. Additionally, we conduct a comparative analysis using an atomic-like Hamiltonian model for noninteracting magnetic ions under various magnetic fields. Our findings indicate that at high temperatures, the magnetic susceptibility predictions from the noninteracting model correspond with those from our more comprehensive DFT + CFT + Δ or SPM + CFT approaches, while at lower temperatures, notable differences emerge. The theoretical predictions made by our interacting DFT + CFT + Δ and SPM + CFT methods align with the experimental data cited in [16], thereby reinforcing the credibility of our approach.

Abbreviations used in this paper are listed and defined in the last section of Ref. [40], titled LIST OF ABBREVIATIONS on pages 6 and 7, providing a quick reference for readers.

II. THEORY AND METHODS

The three approaches (C, R, A), originally classified in Ref. [32], have been widely used in the literature for fitting the optical spectra of rare-earth ions in S_4 site symmetry, where C, R, and A stand for complete, reduced, and approximated, respectively. For their origin and applicability, see the work [32]. It is important to note that the intricate properties of

CF Hamiltonians, $\hat{H}_{CF}$, stem from the algebraic symmetry of these Hamiltonians. This symmetry is accounted for by the Noether theorem [34] in cases of continuous site symmetry, including S_4 site symmetry, which has been extensively studied for trivalent rare-earth (R^{3+}) ions in LiYF$_4$ [33].

The C-approach employs a complete set of S_4 symmetry CFPs (C-CFP set), while the R-approach utilizes a reduced set, with one parameter set to zero (R-CFP set). The A approach, in contrast, adopts an approximated higher D$_{2d}$ symmetry, balancing reduced computational complexity with significant accuracy.

A note of caution is pertinent: C-CFP sets reported for specific ion-host systems, derived from optical spectra fitting, may be numerically distinct, as they can correspond to different local minima. This makes these sets not directly comparable. In contrast, the R-CFP set, which is unique and corresponds to the global minimum, can be directly compared. There has been some lack of awareness among authors regarding the intricate features of the C- and R-approaches. It was concluded in Ref. [32] that determining all seven independent CFPs in S_4 symmetry solely from fitting the optical spectra of f^n ions is not feasible. Reference [32] also explored the use of methods such as the irreducible tensor method, the point charge model, and the SPM for determining the CFPs of rare-earth ions in low symmetry environments.

A. Hamiltonian for a magnetic ion in the crystal

The physical model Hamiltonian, $\hat{H}$, including the Zeeman electronic interaction term, operating on $4f$ states of LiTmF$_4$ is as follows [41,42]:

$$\hat{H} = \hat{H}_A + \hat{H}_{CF} + \tilde{H}_Z, \tag{1}$$

where $\hat{H}_A$ is the free ion Hamiltonian [43], $\hat{H}_{CF}$ is the CF Hamiltonian and $\tilde{H}_Z$ is the (effective) Zeeman electronic interaction. Rudowicz and Karbowiak have reviewed various notations and forms of the CF Hamiltonians as well as elucidated fundamental differences between the physical CF Hamiltonians and the effective spin Hamiltonians, which are not well recognized in literature [44]. For compact and expanded forms of Wybourne notation see Eqs. (2)–(4) in Ref. [44] and the review [45]. In this paper, we choose the compact form of $\hat{H}_{CF}$ in Wybourne notation as follows [46–50]:

$$\hat{H}_{CF} = \sum_{k=0}^{k_{max}} \sum_{q=-k}^{k} B_{kq} \hat{C}_q^{(k)}, \tag{2}$$

where B_{kq} are the CFPs, and $\hat{C}_q^{(k)}$ (with $k_{max} = 6$ and $-k < q < k$) are spherical tensor operator of rank k. $\hat{C}_q^{(k)}$, acting on $4f$ electrons of the Tm ion, can be expressed in terms of the spherical harmonics $\hat{Y}_q^k$ as

$$\hat{C}_q^{(k)} = \sqrt{\frac{4\pi}{2k+1}} \, \hat{Y}_q^k. \tag{3}$$

In Eq. (1), instead of the Zeeman electronic interaction for free atoms, $\hat{H}_Z$:

$$\hat{H}_Z = \mu_B \boldsymbol{B}. \sum_i (\boldsymbol{l}_i + 2\boldsymbol{s}_i), \tag{4}$$

the effective, $\tilde{H}_Z$ for paramagnetic ions in the solids must be used [24]:

$$\tilde{H}_Z = \mu_B \boldsymbol{B}.\boldsymbol{g}.\tilde{\boldsymbol{S}}, \tag{5}$$

where $\mu_B = e\hbar/2\mathfrak{m}_e c$, $\boldsymbol{B}$ is an external magnetic field, $\boldsymbol{g}$ is the effective Zeeman tensor, $\tilde{\boldsymbol{S}}$ is an effective spin which gives the degeneracy of levels to be $2\tilde{S} + 1$ [24]. Similarly, $\tilde{H}_Z$ for paramagnetic $4f^N$ ions in the solid is

$$\tilde{H}_Z = \mu_B \boldsymbol{B} \cdot \boldsymbol{g} \cdot \boldsymbol{J}, \tag{6}$$

where $\boldsymbol{J}$ is the total angular momentum number. In Eqs. (5) and (6) $\boldsymbol{g}$ is tensor due to the anisotropic angular momentum and magnetic moment in crystals in contrast to atoms [51]. We assume that the CF levels are so well separated that the different $\boldsymbol{J}$ are not mixed either by magnetic field or by CF. Figure 7 of Ref. [36] with Fig. 3 confirm the validity of this assumption. The matrix form of Eq. (6) can be written as

$$\hat{H}_Z = \mu_B (B_x \ B_y \ B_z) \begin{pmatrix} g_{xx} & g_{xy} & g_{xz} \\ g_{yx} & g_{yy} & g_{yz} \\ g_{zx} & g_{zy} & g_{zz} \end{pmatrix} \begin{pmatrix} J_x \\ J_y \\ J_z \end{pmatrix}, \tag{7}$$

can be expanded as

$$\begin{aligned} \hat{H}_Z = \mu_B (&g_{xx}B_x J_x + g_{yy}B_y J_y + g_{zz}B_z J_z \\ &+ g_{xy}B_x J_y + g_{yx}B_y J_x + g_{yz}B_y J_z \\ &+ g_{zy}B_z J_y + g_{zx}B_z J_x + g_{xz}B_x J_z). \end{aligned} \tag{8}$$

The $\boldsymbol{g}$ tensor in Eq. (8) can be expressed in the principal axes (x, y, z), i.e., with the nondiagonal elements eliminated. Hence, in this case $\hat{H}_Z$ can be simplified as

$$\hat{H}_Z = \mu_B (g_{xx}B_x J_x + g_{yy}B_y J_y + g_{zz}B_z J_z). \tag{9}$$

Note that the values g_{vv} in Eq. (9) differ from those in Eq. (8), where $v = x, y, z$. The $\boldsymbol{g}$ tensor depends on the direction of the external magnetic field as

$$g^2 = l^2 g_{xx}^2 + m^2 g_{yy}^2 + n^2 g_{zz}^2, \tag{10}$$

where, l, m, and n are the cosines of the applied magnetic field direction with respect to the principal axes. In an axial symmetry,

$$g^2 = g_\parallel^2 \cos^2 \theta + g_\perp^2 \sin^2 \theta, \tag{11}$$

where θ is the angle between the magnetic field and z axis [24]. In Eq. (11), $g_\parallel \equiv g_{zz}$ and $g_\perp \equiv g_{xx} = g_{yy}$.

By considering the above relations and applying the second-order perturbation theory to the Eq. (1), we can establish the relationship between the energy of the ith doublet states and the magnetic field as follows [52]:

$$\varepsilon_i(\boldsymbol{B}) = \varepsilon_i(0) \pm \tfrac{1}{2}\mu_B \boldsymbol{B} g_i(\hat{n}) - \tfrac{1}{2}\boldsymbol{B}\chi_i^{vV}\boldsymbol{B}, \tag{12}$$

where $\hat{n} = \frac{\boldsymbol{B}}{|\boldsymbol{B}|}$, $\varepsilon_i(0)$ is the energy when magnetic field approaches to zero, and χ_i^{vV} is the Van Vleck susceptibility. For the ith non-Kramers singlet states the linear term omit and the dependence of energy to the magnetic field is as follows:

$$\varepsilon_i(\boldsymbol{B}) = \varepsilon_i(0) - \tfrac{1}{2}\boldsymbol{B}\chi_i^{vV}\boldsymbol{B}. \tag{13}$$

In Eq. (12), $\boldsymbol{g}_i$ tensor and χ_i^{vV} tensor along with their components, and in Eq. (13), χ_i^{vV} tensor and its components,

are dependent on the energy level i because they are influenced by the specific electronic configurations and the crystal field environment of each state. The dependence of the g-factor and Van Vleck susceptibility on the energy level can be realized by examining the underlying quantum mechanical principles and their manifestations in solid-state systems. Chibotaru *et al.* [51], by introducing a unique definition of the Zeeman-splitting g_i tensor of a Kramers doublet, have provided significant insights into these dependencies. This is well-illustrated in Fig. 3 of their paper and its accompanying discussion. Different singlet and doublet states have distinct energy levels and wave functions, leading to variations in how these states interact with the external magnetic field. The g factor, as a measure of the splitting of energy levels in a magnetic field, can vary based on the state's angular momentum and the crystal field effects specific to that state. Similarly, the Van Vleck susceptibility, representing the second-order contribution to the magnetization from virtual transitions to excited states, can also depend on the specific electronic structure and the energy separation between the ground and excited states for each singlet or doublet states. In this work, we will report these values for different states to highlight how the magnetic properties vary across the energy levels of the system. Each state, being subject to different crystal field splittings and electronic environments, exhibits unique magnetic responses, which are reflected in their respective g factors and Van Vleck susceptibilities. This state-specific dependence is crucial for accurately describing the magnetic behavior of the system and ensuring that our theoretical predictions align with experimental observations.

Using quadratic regression, we can determine the susceptibility and the g_i effective Zeeman tensor. To this end, we first, calculate the eigenenergies ε_i in the external magnetic field. The magnetic moment of the ith eigenstate in Bohr magnetons in ν direction is

$$m_{i,\nu} = -\frac{d\varepsilon_{i,\nu}}{dB_\nu}, \tag{14}$$

where ν denotes the direction of the external $\boldsymbol{B}$ applied either perpendicular ($\perp$, [100] direction) or parallel ($\parallel$, [001] direction) to the tetragonal axis, to analyze its orientation relative to the crystallographic axis.

Utilizing Boltzmann statistics, we calculate the temperature-dependent magnetic moment for the Tm^{3+} ion as

$$M_\nu(T) = \frac{\sum_i m_{i,\nu} e^{-\varepsilon_{i,\nu}/k_B T}}{\sum_i e^{-\varepsilon_{i,\nu}/k_B T}}, \tag{15}$$

where k_B denotes the Boltzmann constant. Subsequently, the magnetic susceptibility χ_ν is calculated using:

$$\chi_\nu(T) = \frac{\partial M_\nu}{\partial B_\nu}, \tag{16}$$

facilitating the examination of its temperature and directional dependence.

In this section, we have presented a Hamiltonian model for a magnetic ion in LiTmF$_4$, integrating CF and Zeeman interactions. Additionally, in Sec. SIII in Ref. [40], we discuss a noninteracting R^{3+} ion system under an external field, providing an essential benchmark for comparison. This

noninteracting case, serving as an extreme limit, allows us to validate our results for the interacting system in LiTmF$_4$. By comparing these two scenarios, we gain a more comprehensive understanding of LiTmF$_4$'s magnetic behavior, particularly in different external conditions.

B. Conserved quantities (CQs)

In this section, we utilize the concept of CQs [32,34] and the implications of Noether's theorem [33] to investigate the trends in the reported CFPs datasets for R^{3+} ions in LiYF$_4$. This approach integrates the extensive previous works [32–34] with the current research objectives. These datasets were obtained by either theoretical calculations or experimental optical and magnetic spectroscopy data utilizing one of the three approaches (C, R, A). This analysis indicates that although the first-order CQs may be expected to be mutually close for a given ion in different datasets, these CQs exhibit significant differences, while the second-order CQs exhibit less variation. The paper [33] also discusses the challenges in accurately fitting experimental data to determine CFPs, which can have large dispersions from the average. To address this problem, a two-pronged approach was proposed [33], involving a systematic quantum mechanical *ab initio* analysis and systematic refitting of experimental data with multiple starting points using the multiple correlated fitting technique (MCFT) [53].

As detailed in Refs. [33,34], for S$_4$ symmetry the first-order CQs are the CFPs with $q = 0$, i.e., B_{20}, B_{40} and B_{60}. Furthermore, the second-order CQs in Wybourne notation are as follows:

$$|\boldsymbol{v}_{44}| = 2^{1/2}(\{\Re[B_{44}]\}^2 + \{\Im[B_{44}]\}^2)^{1/2},$$

$$|\boldsymbol{v}_{64}| = 2^{1/2}(\{\Re[B_{64}]\}^2 + \{\Im[B_{64}]\}^2)^{1/2},$$

$$\boldsymbol{v}_{44}.\boldsymbol{v}_{64} = |\boldsymbol{v}_{44}||\boldsymbol{v}_{64}| \cos\left(\beta_{44}^{64}\right). \tag{17}$$

The angle β_{44}^{64} offers valuable insights into the detailed electronic environment and interactions within the crystal lattice, which are critical for understanding and predicting the material's properties, such as magnetization.

C. Superposition model of CF parameters

For independent verifications of the *ab initio* calculated CFPs, we also employ the SPM to calculate the CFPs, denoted as SPM/CFPs. In the SPM/CFPs analysis, the CFPs are calculated using detailed structural data pertaining to the Tm^{3+} centers, listed in Table S1 in Ref. [40], and complemented by the depiction of the unit cell of LiTmF$_4$ illustrated in Fig. S1. These calculations are grounded on general formulas established in prior studies [54–56].

In accordance with the Wybourne notation for the CFPs (B_{kq}) [44], B_{kq} can be calculated as follows:

$$B_{kq} = \sum_i \bar{A}(R_i) K_{kq}(\theta_i, \phi_i), \tag{18}$$

where, the coordination factors $K_{kq}(\theta_i, \phi_i)$ are explicit functions of the angular position of the ith ligand ion [57]. The intrinsic parameters $\bar{A}(R_i)$ are given by

$$\bar{A}(R_i) = \bar{A}(R_0)(R_0/R_i)^{t_k}. \tag{19}$$

TABLE I. Comparative analysis of CQs, as defined in [33], for the thulium ion (Tm^{3+}) in lithium thulium fluoride ($LiTmF_4$) and lithium yttrium fluoride doped with thulium ($LiYF_4$:Tm^{3+}). The first-order quantities (with $q = 0$), which include B_{20}, B_{40}, and B_{60}, are expressed in cm^{-1}. The second-order quantities comprise the magnitudes $|v_{44}|$ and $|v_{64}|$ (in cm^{-1}), and the angle β_{44}^{64} (in degrees), indicating inter-vector relationships and orientations in the CF environment.

$LiTmF_4$	B_{20}	B_{40}	B_{60}	$|v_{44}|$	$|v_{64}|$	β_{44}^{64}	Method	Ref.
	384	−660	39	1149	943	11.19	DFT	[36]
	373	−699	−30	1190	907	7.53	average (DFT+Exp.)[a]	This work
	373	−699	39	1175	1359	5.84	SPM[b]	This work
	367	−716	−64	1226	902	11.40	Exp.	[35]
	368	−720	−65	1195	875	0.01	Exp. [c]	[16]
$LiYF_4$:Tm^{3+}	375	−630	−46	1069	1621	17.83	SPM	This work
	357	−630	−46.54	1319	786	1.80	average (Exp. + theory)	This work
	359	−608	173	1194	890	0	Exp.	[37]
	−475	−721	233	1379	**1158**	**180.09**	Exp. [d]	[33,67]
	348	−639	−182	1222	907	0	Exp.	[33,67,68]
	364.98	−618.22	−96.19	1594	450	0	Point charge model	[33,69]
	322.58	−625.98	−63.05	1284	849	0	Exp.	[33,69]
	342	−664	−72	1267	847	10.80	Exp.	[31]
	399	−627	−39	1291	775	0	Exp.	[70]

[a]This represents the averaged values of CFPs and CQs, calculated by utilizing the available sets of experimental and computed CFPs, excluding those derived from the SPM.

[b]The SPM/CFPs are calculated by matching the predicted CFP and CQ values with the averaged ones, as detailed in footnote a.

[c]For an explanation of the renormalized CFPs set, as discussed in Ref. [16], refer to Sec. IV E 1.

[d]This dataset was excluded from the average calculation because the values highlighted in bold significantly differ from those in the other datasets.

In this equation, R_i signifies the distance between the d^N ion and the ligand ion, $\bar{A}(R_0)$ is the intrinsic parameter associated with the reference distance, R_0, for a given ion-host system, and t^k represents the power-law exponent.

To substantiate our findings, we have carried out calculations of the CFPs B_{kq} based on the SPM utilizing Eq. (18), Eq. (19), and crystal structure in Table S2, results of which are consolidated in Table S3 including CFPs for Tm^{3+} ion in $LiTmF_4$ and $LiYF_4$:Tm. These calculated parameters exhibit a noteworthy agreement with the average CFPs documented in Table I calculated using *ab initio* DFT + CF approach, as to be discussed in Sec. IV A, thereby providing a reliable and independent verification of the calculated CFPs.

III. DETAILS OF COMPUTATIONS

For the parameters B_{kq} in the CF Hamiltonian, as expressed in Eq. (2), we utilize our calculated nonzero independent CFPs, as tabulated in Table I of Ref. [36] and briefly described here. First, we calculate the electronic structure based on the full-potential augmented plane waves (FP-APW) plus local orbitals method employing the PBE-GGA functional [58], as implemented in WIEN2K [28]. In the first step, we confine the $4f$ electrons into the core region and perform open core calculations [36,59–61]. In the second step, we release the confined $4f$ electrons from the core region to the valance state and employ the electron potential, obtained in the previous step, to solve the eigenvalue problem in a non-self-consistent calculation. We use the experimental lattice parameters to construct the crystal structure. We let $4f$ orbitals of Tm hybridize with the $2p$ and $2s$ orbitals of the ligands using adjustable parameter Δ, see Ref. [62] and Secs. III and IV A of Ref. [36] for details. In the next step, we transformed the Bloch states

to the Wannier functions using WANNIER90 [63] package to extract the local $4f$ Hamiltonian in the Wannier bases, see Appendix C of Ref. [36]. Subsequently, to determine CFPs, we expand the local $4f$ Hamiltonian in the terms of the spherical tensor operators, see Eq. (C10) in Appendix C of Ref. [36]. The comparison between the Wannier-interpolated band structure and the one computed by DFT, as illustrated in Fig. 1, highlights the precision and accuracy of our computational approach. Given the small energy scales involved, it is crucial that each step of our simulation is well-converged within a reasonable threshold. The agreement between the
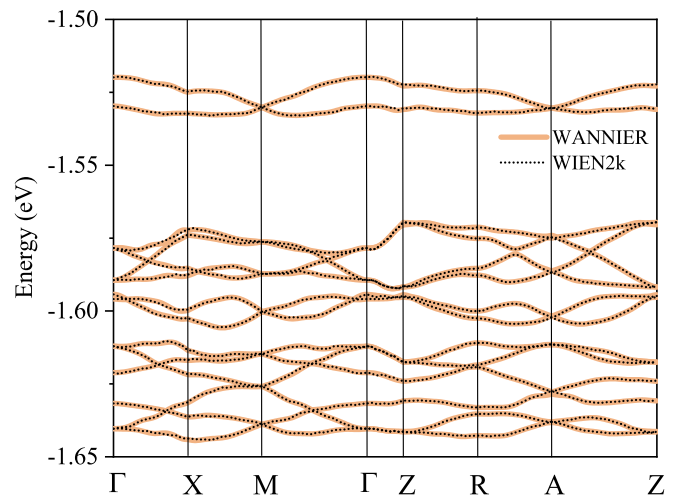

FIG. 1. Comparison of the band structures obtained directly from the second step of the DFT calculations (dotted lines) using WIEN2K [28] and those derived from the Wannier-interpolated Hamiltonian (solid lines) for the $4f$ subspace using WANNIER90 [63].

band structures obtained from WIEN2K [28] and those derived from WANNIER90 [63] underscores the reliability of our Wannierization process. The overlap of the band structures from both methods validates our procedure, indicating that the Wannier functions accurately capture the essential physics of the system. Any significant discrepancy between the two band structures would suggest potential inaccuracies in the Wannierization or the initial DFT calculations. However, the close match confirms that our computational methods are robust and accurate even for the fine energy scales considered. The minimal deviations between the two band structures suggest a very low noise level in the Wannierization, ensuring that the Wannier-interpolated Hamiltonian accurately represents the system's electronic structure. This low noise level is crucial for resolving tiny energy variations. From the initial FP-APW plus local orbitals method calculations with WIEN2K to the transformation of Bloch states to Wannier functions, each computational step was thoroughly converged. The accurate description of the electronic structure implies that the calculated energy variations and related physical properties can be expected to match closely with experimental observations.

Total energy convergence was achieved using a mesh of 200 special k points, corresponding to a $5 \times 5 \times 5$ grid in the Monkhorst-Pack scheme [64], within the irreducible wedge of the first Brillouin zone. Nevertheless, to enhance the accuracy of the crystal field calculations, a denser k mesh of 1000 specific k points within the irreducible wedge of the first Brillouin zone was employed. This denser mesh corresponds to a $10 \times 10 \times 10$ grid in the Monkhorst-Pack scheme [64]. Using this finer mesh, the total energies in the final two iterations of the self-consistent field calculations were determined to be $-55\,958.76327838$ and $-55\,958.76327830$ Ry. The unit of the crystal field parameters B_{kq} in Eq. (2) is the same as that of the crystal field Hamiltonian $\hat{H}_{\mathrm{CF}}$, i.e., energy, while the operators $\hat{C}_q^{(k)}$, as expressed in Eq. (3), are dimensionless. Consequently, the convergence threshold for total energy and CFPs is $|\Delta E| = 0.00000008\,\mathrm{Ry} = 0.00108\,\mathrm{meV} \approx 0.001\,\mathrm{meV}$. In Sec. IV B, we will use this convergence threshold and ensure that our results are within the accuracy of our calculations. To this end, the energy variations of the singlet and doublet states, $|\Delta \varepsilon_i| = |\varepsilon_i(B = 1\,\mathrm{T}) - \varepsilon_i(B = 0\,\mathrm{T})|$ in meV, will be compared with the accuracy of our total energy and CFP calculations ($|\Delta E| = 0.001\,\mathrm{meV}$). Furthermore, to ensure that they can be also practically resolved in experiments, we will compare energy variations with the experimental half width $\delta E = 0.008\,\mathrm{cm}^{-1}$ (0.000992 meV), as reported by Klimin *et al.* in Table I of Ref. [31].

The radii of the muffin-tin spheres are chosen to be 1.56, 2.26, and 1.94 for Li, Tm, and F atoms, respectively. For the expansion of the wave functions, $\mathrm{R_{MT}K_{max}}$ is optimized to be 8, and the periodic charge density and potential are Fourier expanded up to $G_{\mathrm{max}} = 13\,(\mathrm{Bohr})^{-1}$. In the first step, to separate the valence electrons from the core electrons, we select the separation energies to be $-8\,\mathrm{Ry}$.

Building on the approach described previously, we now detail the specific methods used to apply the *ab initio* calculated CFPs in our analysis. Since different approaches can result in various sets of CFPs, we specifically use the *ab initio* calculated CFPs to determine the eigenvalues. These CFPs

are used as input for diagonalization of the Hamiltonian in Eq. (1) with the Zeeman term replaced by that in Eq. (6). Our focus is on the *ab initio* method, hence the utilization of these calculated CFPs. To this end, we follow the method proposed in Refs. [62,65], as implemented in the CFP code, which is a modified version of the lanthanide package [66]. For the parameters of the free ions Hamiltonian, $\hat{H}_{\mathrm{A}}$, we use the values reported for Tm^{3+} in $\mathrm{LaF_3}$ by Carnall *et al.* [42]. This is justified due to rotational invariance of $\hat{H}_{\mathrm{A}}$, which makes these values almost material independent. We also use Eq. (4) for the Zeeman interaction term. In this way, we determine the components of the $\boldsymbol{g}_i$ tensor, $g_{i\perp}$ and $g_{i\parallel}$, and the Van Vleck susceptibility, $\chi_{i\perp}^{vV}$ and $\chi_{i\parallel}^{vV}$, using the energy eigenvalues in various external magnetic fields. Finally, we reproduce the temperature dependencies of the magnetization and susceptibility of Tm^{3+} ion in $\mathrm{LiTmF_4}$.

IV. RESULTS AND DISCUSSIONS

This section is devoted to an investigation of interconnected aspects that reveal the significance of the results only when considered collectively. After presenting the aspects considered in this work and the generalizations made compared to the previous work [36], it will be elucidated how their integration can enhance the study's overall strengths and synergistic effects, demonstrating the power and depth of the approaches.

The following sections explore conserved quantities using calculated CFPs to understand the electronic environment and interactions within the crystal lattice, which are critical for predicting various properties. This validation influences energy level splittings and reinforces the reliability of our study. By examining energy level variations under an external magnetic field, we focus on how field orientation causes distinct energy splits and the differential responses of singlet and doublet states, enhancing our understanding of electronic properties and anisotropy effects. We extrapolate multiplet energies in the absence of a magnetic field using data validated by existing experimental results and theoretical analyses. Additionally, we assess zero-temperature properties, examining how field orientation affects energy level splitting and singlet and doublet state responses through quadratic regression to deepen our understanding of anisotropy and its broader applications while validating our models with existing data, including magnetic properties. Finally, this study also explores how temperature impacts magnetization and susceptibility, using Boltzmann statistics and experimental comparisons to refine our models.

Let us below discuss how the above aspects are studied by generalizing the previous work [36]. In the previous study [36], performed at zero temperature, we used standard DFT to investigate ground state properties. Incorporating nonzero temperatures requires special consideration, as discussed in the Electronic Supplemental Information of Ref. [29]. In this work, we extended our previous study by using a combination of DFT and Boltzmann theories to examine the temperature dependence of the magnetic properties of the system. Additionally, while our earlier work considered the compounds as nonmagnetic systems, we now addressed the challenges of noncollinear magnetic systems by employing statistical

mechanics within the canonical ensemble framework to study the paramagnetic phase. Previously, we investigated multiplet splittings in the absence of an external magnetic field; in this study, we integrated CFT with Zeeman effects to include an external magnetic field in our analysis. Moreover, alongside DFT, we here incorporate the superposition model, integrating it with CFT, Zeeman effects, and statistical mechanics within the canonical ensemble framework. In this work, an analytical approach is also used to verify asymptotic behaviors. By comparing the results of these three approaches—(1) DFT combined with CFT, Zeeman effects, and statistical mechanics; (2) the superposition model combined with CFT, Zeeman effects, and statistical mechanics; and (3) the analytical approach—with each other and with available experimental data, we demonstrate the reliability and robustness of our research. These integrated methods ensure that the findings are comprehensive and reflective of the multifaceted nature of the studied system.

Now is an appropriate time to discuss how the integration of the aspects and generalizations boosts the combined outcomes, revealing the robustness and depth of the methodology. By combining DFT with CFT, Zeeman effects, and statistical mechanics, this study bridges the gap between quantum mechanical modeling and classical statistical approaches. This allows for a more comprehensive analysis of the system's properties and enhances the predictive power of our models under varying conditions, such as temperature changes and external magnetic fields. The use of the superposition model in conjunction with these theories enables us to capture the complex interactions within the crystal lattice more accurately, which is crucial for understanding the magnetic properties and energy level splittings in noncollinear and paramagnetic systems. Additionally, incorporating an analytical approach to verify asymptotic behaviors provides robust validation of our theoretical predictions, ensuring accuracy across a broader range of scenarios and increasing the reliability and applicability of our research. This work exemplifies the power of interdisciplinary research in advancing scientific knowledge. By integrating concepts from condensed matter physics, quantum mechanics, and statistical physics, we create a cohesive framework that addresses complex phenomena from multiple perspectives. This holistic approach is essential for developing new technologies, such as advanced magnetic materials and low-temperature applications, which rely on a deep understanding of underlying physical principles. Furthermore, our findings have the potential to influence various scientific domains, including the design of novel magnetic storage devices and sensors, advancements in spintronics and quantum computing. By addressing these interdisciplinary challenges, our research paves the way for future innovations and technological breakthroughs.

Considering collectively the above concepts, including the integration of different theories and their close relationship with our previous work [36], demonstrates how, in the following sections, we will address the inherent complexities of the problem caused by paramagnetism, incorporate temperature into the standard temperature-independent DFT, and combine DFT with CFT under an external magnetic field, all in the simplest possible manner. The theoretical approaches discussed and used in this work absorb these complexities and simplify

them, enabling a highly accurate analysis and understanding of the problem in the most transparent way possible while considering all relevant factors. These points elucidate that this study adopts a dual focus approach, concentrating first on the theoretical approaches used and second on the material properties of $LiTmF_4$, to make solving the problem simple and feasible.

A. Analysis of conserved quantities

We collected the CFPs and CQs for the $LiTmF_4$ dataset from Table I of Ref. [36], along with datasets from Refs. [16,35] and calculations based on Eq. (17). These were then compared with data for $LiYF_4:Tm^{3+}$ from Ref. [33], and further augmented with relevant datasets found in Refs. [31,70]. Since various notations and symbols [44,45] have been employed for CFPs reported for Tm^{3+} ion in $LiTmF_4$, we have verified that the CFPs complied in Table I conform to the convention used in Eq. (2), and thus are expressed in Wybourne notation. The dataset of Ref. [16] has been converted into Wybourne notations based on Eq. (B1) and Table VII of Ref. [36] and considering Refs. [44,71]. We have also performed the process of averaging by considering all available CFPs sets (except SPM/CFP) to analyze the dispersion of the sets from average.

For a comparative analysis, we have compiled in Table I the CQs for a comparative analysis of CQs to present a detailed compilation of the CQs for the thulium ion (Tm^{3+}) in two distinct compounds: lithium thulium fluoride ($LiTmF_4$) and lithium yttrium fluoride doped with thulium ($LiYF_4:Tm^{3+}$). The CQs include both first-order (B_{20}, B_{40}, and B_{60}) and second-order ($|v_{44}|$, $|v_{64}|$, and β_{44}^{64}) quantities, where the first-order ones are expressed in cm^{-1} and represent components of the CFPs, while the second-order quantities, also in cm^{-1} except for β_{44}^{64} (in degrees), relate to the magnitude and angular relationships of the CFPs vectors. Data are sourced from various studies, as reviewed above and cited in Table I, employing different methodologies, including DFT, SPM, and experimental measurements (Exp.). This comprehensive dataset facilitates a comparison between $LiTmF_4$ and $LiYF_4:Tm^{3+}$ in terms of the consistency and dispersion of CQs, as well as highlights the effect of the methods employed on the determined CFP values. References are provided for each data set, allowing for an in-depth examination of the origin and context of these values. Subsequently, we compared the trends in CQs of two categories.

Analysis of the values in Table I reveals what follows. For $LiTmF_4$, the B_{20} parameter shows the least dispersion from the average, suggesting a higher reliability in its determination. Conversely, the B_{60} parameter exhibits the largest dispersion, indicating potential uncertainties in its determination or sensitivity to the method employed. Generally, the dispersion of average values in $LiTmF_4$ is lower than that in $LiYF_4:Tm^{3+}$ for most CQs, which could imply a more consistent or accurate determination of CQs in the former compound.

B_{20} parameter demonstrates the largest consistency across different methods, with values ranging narrowly from 367 to 384 cm^{-1}. This consistency might indicate a robustness of B_{20} against different calculation or measurement techniques. B_{40}

and B_{60} parameters show more variation. Particularly, B_{60}'s variation, from -65 to 39 cm^{-1}, highlights the challenges in accurately determining higher-order CFPs. Such variation could be due to the sensitivity of these parameters to the local environment and computational or experimental methods. $|v_{44}|$ and $|v_{64}|$ values: The magnitudes of these vectors v_{44} and v_{64}, $|v_{44}|$ and $|v_{64}|$, also vary, but not as drastically as B_{60}. The variations are indicative of differences in the electronic environment sensed by the Tm^{3+} ion in different studies or methods. β_{44}^{64} angle shows significant variation, from $0.01°$ to $11.40°$. The angle β_{44}^{64} essentially quantifies the relative phase or orientation between the CF effects described by the v_{44} and v_{64} vectors. This angle can influence how these effects combine or interfere, thereby affecting the overall energy level splitting and, consequently, the physical properties of the ion in the crystal lattice. Therefore significant variation in this angle across different studies or methods suggests that the relative orientation of these CF effects is sensitive to the specific local environment of the Tm^{3+} ion or the details of the computational and experimental approaches used. Changes in the local symmetry, distortions in the crystal lattice, or differences in the way the electronic orbitals are modeled can all lead to different orientations of these CF components, as captured by the angle β_{44}^{64}. Thus this variation might be related to the orientation of the electronic orbitals, which can be sensitive to the local CF and the measurement or calculation methods.

To enhance our understanding of how the local environment affects CFPs and CQs, we present the percentages of relative changes in these parameters, $\frac{\text{CFP}-\text{CFP}_0}{\text{CFP}_0} \times 100$ and $\frac{\text{CQ}-\text{CQ}_0}{\text{CQ}_0} \times 100$, with respect to the percentage of relative volume change, $\frac{V-V_0}{V_0} \times 100$, in Fig. 2. Here, CFP$_0$, CQ$_0$, and V_0 are the values of CFP, CQ, and V evaluated at zero pressure, respectively. The data clearly demonstrate distinct behaviors among different CFPs and CQs in response to relative volume changes. Firstly, B_{20} exhibits the least relative change in response to relative volume changes compared to the other CFPs and CQs, as shown in Fig. 2(a). This minimal change suggests that B_{20} is less sensitive to changes in the local environment, which may explain its minimal dispersion from the average. In contrast, parameters such as B_{60} and $\Re[B_{64}]$ show more significant relative changes, indicating a higher sensitivity to the relative volume changes. Furthermore, Fig. 2(b) highlights that relative changes in second-order conserved quantities (CQs), β_{44}^{64}, $|V_{44}|$, and $|V_{64}|$, as expressed in Eqs. (17), are more pronounced during compression than during expansion. This asymmetry suggests that the local environment's response to volumetric strain is nonlinear, particularly under compressive strain. The pronounced relative change in β_{44}^{64} during compression, compared to expansion, underscores its high sensitivity to changes in the local environment. To provide quantitative evidence supporting our argument, the relative percentage changes of CFPs and CQs with respect to volume change are analyzed. For instance, B_{20} varies by less than 10% across the entire range of volume changes, whereas B_{60} and $\Re(B_{64})$ vary by approximately 20% to 30%. Similarly, β_{44}^{64} shows a significant variation of up to 30% during compression, compared to about 10% during expansion. These observations quantitatively demonstrate that small changes in lattice constants, bond lengths, or angles can lead to significant relative
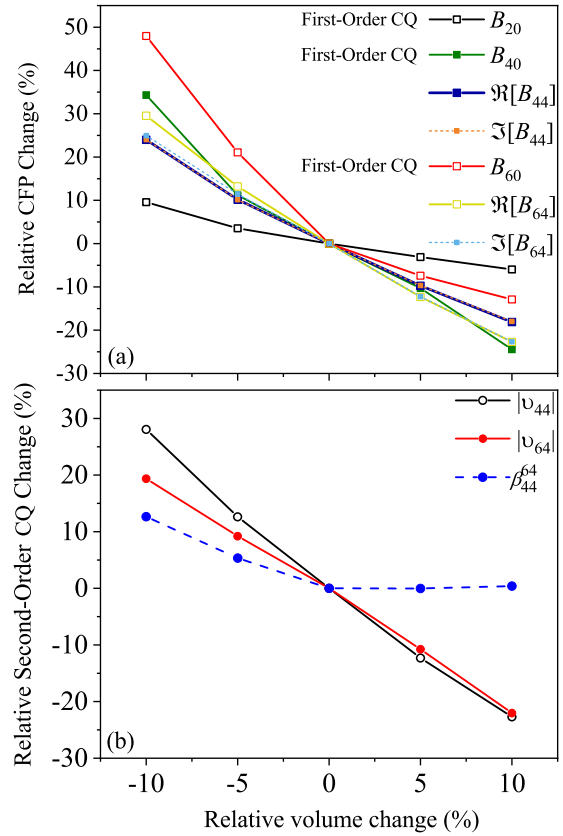

FIG. 2. Dependencies of (a) crystal field parameters (CFPs) B_{20}, B_{40}, $\Re[B_{44}]$, $\Im[B_{44}]$, B_{60}, $\Re[B_{64}]$, and $\Im[B_{64}]$, including first-order conserved quantities (CQs) B_{20}, B_{40}, and B_{60}, and (b) second-order conserved quantities (CQs) $|V_{44}|$, $|V_{64}|$, and β_{44}^{64}, on relative volume change (%). The plots illustrate the relative changes (%) in these parameters under contractive and expansive strain, highlighting the distinct behaviors of different CFPs and CQs. The lines shown in the figures are visual guides for better clarity only.

changes in calculated CFPs and CQs. The nonlinear response, particularly under compressive strain, indicates that the local environment plays a crucial role in determining the values of these parameters. Therefore the local structural changes due to relative volume variations can significantly influence the CFPs and CQs, justifying the sensitivity of these parameters to the local environment.

The data for LiYF$_4$:Tm^{3+} shows a greater range of values compared to LiTmF$_4$, especially for B_{20} and B_{60}. This could be due to intrinsic differences in the crystal structure or local environment in the two compounds. Notably, some values, such as -475 cm^{-1} for B_{20} and $180.09°$ for β_{44}^{64}, stand out as outliers. These values are significantly different from other datasets and might be indicative of experimental anomalies or specific conditions under which these measurements were taken.

The variation in CQs across different methods suggests a significant influence of the chosen technique on the results. This underscores the importance of method selection and the need for cross-validation across different techniques. The dispersion, especially in higher-order CQs, highlights the challenges in determining these parameters accurately. This
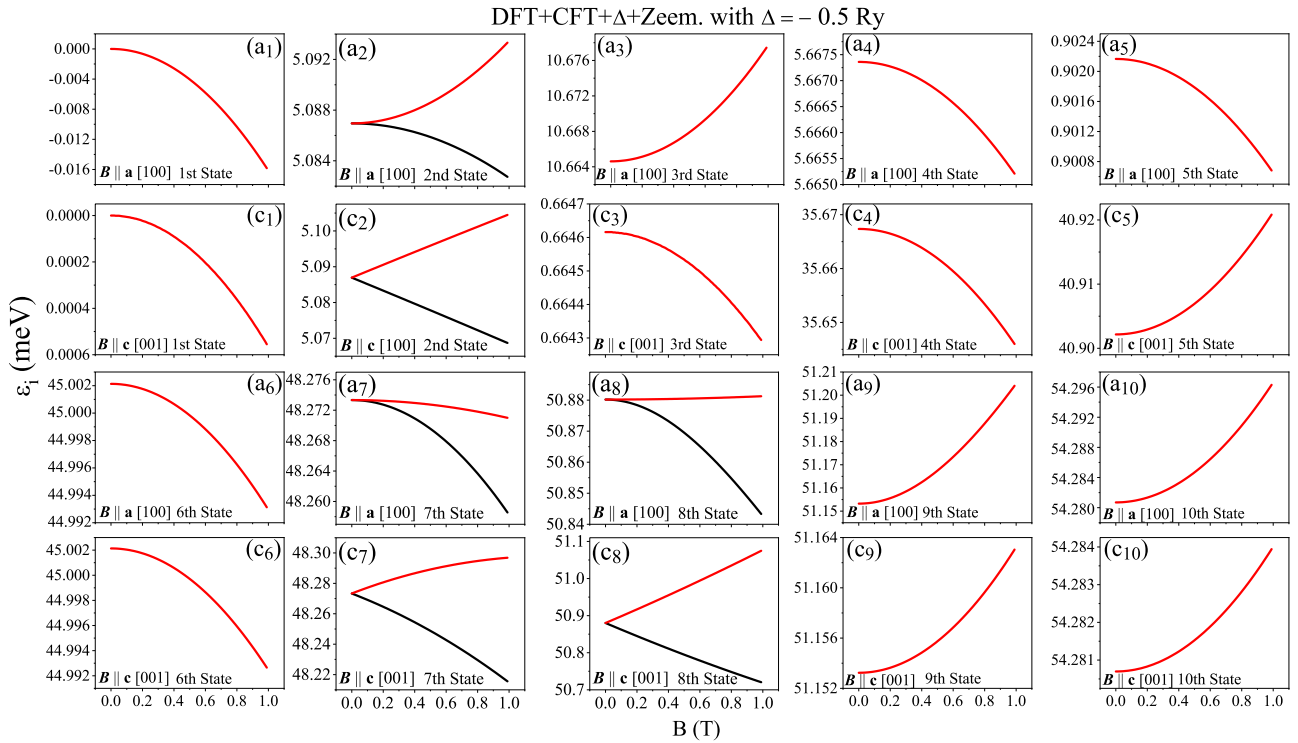
FIG. 3. Variation of the energy levels ε_i of singlet (Γ_1, Γ_2) states (red curves) and doublet (Γ_3, Γ_4) states (red and black curves) in the ground state $^3H_6$ multiplet of Tm^{3+} ion in $LiTmF_4$, as a function of the external magnetic field $\boldsymbol{B}$, ranging from 0 to 1 T. The field is applied along the [100] axis (panels a_1 to a_{10}) and the [001] axis (panels c_1 to c_{10}). The state index i in ε_i varies from 1 to 10, corresponding to the indices of the panels a_i and c_i.

could have implications for theoretical models that rely on these values, potentially affecting the accuracy of predictions or simulations.

Overall, our analysis underscores the complexity of accurately determining CQs in compounds with S_4 site symmetry. The observed variability points to the need for careful selection and validation of methods, as well as the importance of understanding the influence of the local environment on these parameters.

This analysis suggests avenues for further research, particularly in improving the accuracy of higher-order CFPs and understanding the underlying causes of variability in CQs. Advanced computational methods or more refined experimental techniques might be required to achieve this.

In summary, for $LiTmF_4$, the B_{20} parameter exhibits the least dispersion from the average, while the B_{60} parameter shows the largest dispersion. This may indicate that the sixth-rank CFPs are least reliably determined. We also notice that the dispersion of the average values in $LiTmF_4$ is generally lower compared to $LiYF_4:Tm^{3+}$ for most of the CQs. Thus our findings support the predictions [33] that *ab initio* calculations can enhance the accuracy of CFPs datasets.

B. Multiplet energies of Tm^{3+} ions in $LiTmF_4$ under the influence of an external magnetic field

In this section, we explore the variations of energy levels of Tm^{3+} ions in $LiTmF_4$ crystal with an external magnetic field. By employing CFT to discern the nature of magnetic splitting, our in-depth analysis, as illustrated in Fig. 3, provides crucial

insights into the dynamics of multiplet splittings in a magnetic field and their broader implications.

Initially, we apply CFT to calculate the multiplet splittings under an external magnetic field, as depicted in Figs. 3(a_1)–3(c_{10}). We determine the eigenvalues by solving Eq. (1), considering a magnetic field range from 0 to 1 T along the [100] and [001] directions, corresponding to Figs. 3(a_1) to 3(a_{10}) and 3(c_1) to 3(c_{10}), respectively. The indices represent the numbers of the ground states, whose energies are listed in Table II at zero magnetic field. There are ten ground states in total, including seven singlet states and three doublet states, as detailed in Table II.

The energy levels of the singlet states exhibit a parabolic dependence on the magnetic field strength. This is in agreement with the quadratic nature of their Zeeman interaction, as indicated by the presence of B^2 terms in the related Hamiltonian in Eq. (13), which applies to the non-Kramers singlet states. The third and fifth states (which are the second and fourth singlet states, respectively, as labeled in the first column of Table II), show contrasting responses to an increasing magnetic field along the tetragonal axis. Specifically, the energy of the third state decreases, while the fifth state increases, as depicted in Figs. 3(c_3) and 3(c_5), respectively. In contrast, this behavior is reversed when the field is applied perpendicular to the axis, as illustrated in Figs. 3(a_3) and 3(a_5), respectively. In light of these observations, it becomes evident that the magnetic field orientation plays a crucial role in the splitting of energy levels, with distinct behaviors emerging for fields applied parallel and perpendicular to the tetragonal axis. These results pave the way for a detailed investigation into the

TABLE II. Multiplet energies $\varepsilon_i(0)$ [in meV] of the $^3H_6$ singlet and doublet states for Tm^{3+} in LiTmF$_4$ calculated with an external magnetic field and extrapolated to $B = 0$. We applied quadratic regression on DFT+CFT+Δ results (including a hybridization parameter $\Delta = -0.5$ Ry), labeled as "DFT+CFT+Δ+Zeem.+Reg." and on SPM+CFT results, labeled as "SPM+CFT+Zeem.+Reg." Here "Zeem." refers to Zeeman to indicate that the calculations are performed for $B \neq 0$ and "Reg." refers to regression to indicate that the $\varepsilon_i(0)$ are obtained from $\varepsilon_i(B)$ after regression at $B = 0$. For comparison, our corresponding results previously calculated in the absence of an external magnetic field, denoted as ε_{0i} and labeled as "DFT+CFT+Δ," are included [36]. Experimental (Exp.) and empirical (Emp.) data are from Refs. [17,31,35]. Here, $\varepsilon_i(0)$, calculated in the presence of an external magnetic field but evaluated at $B = 0$, differs from ε_{0i}, which is calculated in the absence of an external magnetic field. The index i represents the state counter. The results are obtained at zero temperature. For further explanations, see Sec. IV C.

Method i	DFT+CFT+Δ+Zeem.+Reg. $\varepsilon_i(0)$ [meV]	States	SPM+CFT+Zeem.+Reg. $\varepsilon_i(0)$ [meV]	States	DFT+CFT+Δ ε_{0i} [meV]	States	Exp. ε_{0i} [meV]	Exp. ε_{0i} [meV]	States	Emp. States	Emp. ε_{0i} [meV]	Emp. ε_{0i} [meV]	Emp. ε_{0i} [meV]	Emp. ε_{0i} [meV]
1	0.000	singlet	0.00	singlet	0.000	singlet	0.00	0.00	singlet	singlet	0.00	0.00	0.00	0.00
2	5.087	doublet	8.20	doublet	5.085	doublet	3.97	3.69	doublet	doublet	3.84	3.94	3.65	4.15
3	10.665	singlet	17.40	singlet	10.663	singlet	7.07	6.82	singlet	singlet	7.69	7.66	7.32	8.30
4	35.677	singlet	37.26	singlet	35.666	singlet		34.1	singlet	singlet	35.58	36.40	34.15	37.79
5	40.902	singlet	47.73	singlet	40.900	singlet		37.82	singlet	singlet	39.18	40.07	42.65	41.94
6	45.002	singlet	51.73	singlet	45.000	singlet			singlet	singlet	45.25	46.14	43.05	48.51
7	48.273	doublet	54.08	doublet	48.272	doublet		42.65	doublet	doublet	47.36	47.56	44.78	51.05
8	50.880	doublet	57.26	singlet	50.878	doublet			doublet	doublet	50.83	51.54	49.00	53.87
9	51.153	singlet	61.21	doublet	51.151	singlet			singlet	singlet	52.20	52.99	50.05	55.61
10	54.281	singlet	68.09	singlet	54.279	singlet			singlet	singlet	54.06	54.61	52.17	57.62
Ref.	This Study		This Study		[36]	[31,35]	[35]	[31]	[17,31,35]		[35]	[17]	[31]	[74]

magnetic anisotropy and its potential effects on the magnetic and electronic properties of the system.

Building upon the foundation of magnetic field-induced energy level splittings, we now turn our attention to the implications of magnetic anisotropy. The following analysis will delve into how these anisotropic behaviors influence the magnetization processes and the potential for utilizing these characteristics in device applications.

There is a clear asymmetry in the response of these states when the magnetic field is applied along the [100] versus the [001] axis. Specifically, the concavity of the energy versus magnetic field strength plots is reversed for the [100] axis compared to the [001] axis. We notice that the concavity of the three and five singlet states is reversed in the two directions. On the other hand, the remaining singlet states exhibit similar behavior in both directions. Figures $3(a_2)$ and $3(c_2)$, depict the splitting of the first excited non-Kramers doublet state, $\Gamma_{3,4}^1$, which is labeled based on the irreducible representations of the S_4 point group.

The doublet states show a more complex dependence on the magnetic field. The energy levels split into two branches for each doublet, with the splitting being more pronounced in the plots corresponding to the [001] axis. The splittings are consistent with the plus and minus signs of the second term in Eq. (12). In the [100] direction, the splitting exhibits quadratic behavior, which is consistent with the third term of Eq. (12) governing the Kramers doublet states. In contrast, the splitting along the [001] direction appears to be more linear, especially noticeable in Figs. $3(c_7)$ and $3(c_8)$. We observe similar splittings in the states of Tb^{3+} and Dy^{3+} ions as reported in [72], which can be considered as indirect confirmation of our observations. This linear behavior aligns with the second term of Eq. (12), indicating distinct magnetic interactions in different crystallographic directions. In conclusion, the changes in the eigenvalues as a function of the magnetic field magnitude exhibit a nonlinear (linear) relationship in the [100] ([001]) direction. These results suggest that the second term in Eq. (12) affects predominantly the splitting for an externally applied magnetic field in the [001] direction, whereas it is less effective for an applied field in the [100] direction. Nevertheless, it is worth noting that the splitting of the states parallel to the tetragonal axis is greater than the splitting perpendicular to it. In the case of an external magnetic field in the [100] direction, the splitting (s) increases as $s \simeq 1.08 \times 10^{-2} B^2$, which is consistent with the findings reported in Ref. [73]. Moreover, it should be mentioned that the splitting increases linearly with the magnetic field magnitude in the direction of the tetragonal axis, and can be seen from $s \simeq B$. Similar to the singlet states, the excited doublet states also exhibit differing multiplet energy behavior when exposed to magnetic fields directed perpendicular or parallel to the tetragonal axis. This inconsistency in behavior is observed in two other excited doublet states as well, as illustrated in Figs. $3(a_7)$, $3(a_8)$, $3(c_7)$, and $3(c_8)$. In particular, for magnetic fields perpendicular to the tetragonal axis, the second and third excited doublet states do not conform to the behavior predicted by Eq. (12) well enough. The anisotropy in the energy levels' response to the applied magnetic field suggests that the magnetic properties of the Tm^{3+} ion in $LiTmF_4$ are highly directional. This anisotropy

is a consequence of the CF environment, which does not treat all spatial directions equally. The variation in the degree of splitting between the different plots reflects the differences in the magnetic interaction strengths along the [100] and [001] axes. The more substantial splitting in the [001] direction indicates a stronger interaction between the magnetic field and the electronic states when the field is aligned with the tetragonal axis. The behavior of the energy levels in response to the magnetic field can be compared with theoretical models that predict the influence of the magnetic field on the electronic states of Tm^{3+}. This comparison can validate the models or in the case of observed discrepancies may suggest refinements to improve the models. The observed splitting patterns and their directional dependence provide insights into the magnetic properties of the material, such as its magnetization behavior, magnetic susceptibility, and anisotropy energy. These properties are crucial for applications in magnetic devices, optical materials, and quantum computing. The behaviors observed in the figure are consistent with phenomena reported in other lanthanide-doped systems [16], as mentioned in the provided discussion, supporting the universality of these magnetic interactions across similar materials.

This study lays a strong foundation for understanding the magnetic properties of $LiTmF_4$, providing key insights and a comprehensive framework for further exploration. To build upon this groundwork, we propose several research directions that can deepen the scientific context and practical applicability of our findings. These avenues, while extending beyond the current scope, offer exciting opportunities to expand the boundaries of our knowledge in this field. Below we outline potential paths for future research, inspired by our work, to further advance the understanding and application of these intriguing materials.

Future research could focus on a deeper understanding of investigating the material's anisotropic magnetic behavior for applications in magneto-optical devices and as qubits in quantum information processing. Additionally, examining the impact of CF symmetry on energy levels and extending the analysis to higher magnetic field strengths would enhance our understanding. Comparative studies with similar materials could reveal broader trends in magnetic behavior, presenting new opportunities for theoretical and practical advancements.

We notice from Fig. 3 that the energy variations versus the magnetic field are very tiny. Before concluding this section, let us ensure that they be practically resolved in simulations or experiments. To this end, we have prepared Table III using Fig. 3. The table presents absolute values of the energy variations $|\Delta\varepsilon_i|$ for both singlet and doublet states under an external magnetic field ranging from 0 to 1 T. The table distinguishes values that are larger than our theoretical convergence threshold for total energy and CFPs ($|\Delta E| = 0.001$ meV) and the experimental half-width $\delta E = 0.008$ cm^{-1} (0.000992 meV). Panels with $|\Delta\varepsilon_i|$ less than the accuracy of our calculations, i.e., 0.001 meV, are the some of the singlet states: a_4 with $|\Delta\varepsilon_i| = 0.00079$ meV, a_5 with $|\Delta\varepsilon_i| = 0.00068$ meV, and a_6 with $|\Delta\varepsilon_i| = 0.00055$ meV. Despite being small, these variations are very close to the convergence threshold for the total energy and CF parameters and thus distinguishable from zero, which indicates that our model can capture fine energy differences. Most

TABLE III. Absolute values of the energy variations of singlet and doublet states, $|\Delta\varepsilon_i| = |\varepsilon_i(B = 1 \text{ T}) - \varepsilon_i(B = 0 \text{ T})|$ in meV, for each panel of Fig. 3, with distinctions for values larger than our theoretical convergence threshold for total energy and CFPs ($|\Delta E| = 0.001$ meV), as reported in Sec. III, and the experimental half width $\delta E = 0.008$ cm^{-1} (0.000992 meV), as indicated in Table I of Ref. [31] and Sec. III. For the doublet states, which are degenerate in the absence of a magnetic field and split into two branches in the presence of the external magnetic field, $|\Delta\varepsilon_i|$ of the upper branch is placed in parentheses. The state index i in ε_i varies from 1 to 10, corresponding to the indices of the panels a_i and c_i in Fi. 3.

Panel	States	$|\Delta\varepsilon_i|$ (meV)	$|\Delta\varepsilon_i| > |\Delta E|$	$|\Delta\varepsilon_i| > |\delta E|$
a_1	singlet	0.016	Yes	Yes
a_2	doublet	0.002 (0.008)	Yes (Yes)	Yes (Yes)
a_3	singlet	0.014	Yes	Yes
a_4	singlet	0.00079 [$\approx$0.001]	No [$\approx$Yes]	No [$\approx$Yes]
a_5	singlet	0.00068 [$\approx$0.001]	No [$\approx$Yes]	No [$\approx$Yes]
a_6	singlet	0.007	Yes	Yes
a_7	doublet	0.013 (0.001)	Yes (Yes)	Yes (Yes)
a_8	doublet	0.035 (0.003)	Yes (Yes)	Yes (Yes)
a_9	singlet	0.053	Yes	Yes
a_{10}	singlet	0.017	Yes	Yes
c_1	singlet	0.00055 [$\approx$0.001]	No [$\approx$Yes]	No [$\approx$Yes]
c_2	doublet	0.016 (0.019)	Yes (Yes)	Yes (Yes)
c_3	singlet	0.00129	Yes	Yes
c_4	singlet	0.020	Yes	Yes
c_5	singlet	0.021	Yes	Yes
c_6	singlet	0.007	Yes	Yes
c_7	doublet	0.056 (0.025)	Yes (Yes)	Yes (Yes)
c_8	doublet	0.157 (0.197)	Yes (Yes)	Yes (Yes)
c_9	singlet	0.012	Yes	Yes
c_{10}	singlet	0.005	Yes	Yes

other states exhibit energy variations significantly larger than the convergence threshold, ranging from 0.002 meV (a_2) to 0.157 meV (c_8). These values are well above both the theoretical threshold and the experimental half-width $\delta E = 0.008$ cm^{-1} (0.000992 meV), as reported in Table I of Ref. [31], ensuring that the calculated variations are not only precise but also practically resolvable in experiments. Doublet states are degenerate in the absence of the magnetic field, while they split into two branches under an external magnetic field. For doublet states, such as in panels a_2, a_7, a_8, c_2, and c_7, the table includes $|\Delta\varepsilon_i|$ values for both branches. The energy differences for the upper branch are placed in parentheses in Table III. These values show significant splitting under the magnetic field, which is consistent with expected physical behavior and can be experimentally observed. The high precision of our calculated energy variations, especially those close to 0.001 meV, demonstrates the robustness of our computational methods. These values confirm that our theoretical model and numerical simulations are capable of capturing small energy shifts with high accuracy, making them reliable for further predictive simulations. The comparison with the experimental half-width $\delta E = 0.008$ cm^{-1} (0.000992 meV) indicates that most of our calculated energy variations are within the resolvable range of experimental techniques. This alignment with experimental parameters supports the practical applicability of our results and suggests that such energy

variations can be measured in laboratory settings using precise spectroscopic methods. The data in Table III confirm the accuracy of our calculations, with many energy variations either exceeding the theoretical and experimental thresholds or being very close to these values. The alignment with experimental resolvability underscores the robustness of our computational approach, ensuring theoretical soundness and experimental verifiability. This coherence reinforces the reliability and practical applicability of our findings. In summary, the detailed investigation of energy level variations in LiTmF$_4$ under an external magnetic field, as presented in this section, is not only integral to our current understanding but also pivotal in guiding future research directions. It underscores the importance of a comprehensive approach that encompasses both diverse theoretical techniques and analysis of experimental data, results of which enable meaningful considerations of practical applications.

C. Multiplet energies of Tm^{3+} ions in LiTmF$_4$ in the absence of an external magnetic field

In light of Sec. IV B regarding the impact of an external magnetic field on LiTmF$_4$, this section focuses on validating our results' accuracy and reliability. Specifically, we analyze how the energy levels of Tm^{3+} ions in LiTmF$_4$ are influenced by the CF in the absence of an external magnetic field. Available experimental, empirical, and theoretical data at $\boldsymbol{B} = 0$ are used for comparison, enabling us to assess the reliability of our findings.

The S$_4$ symmetry of the CF plays a pivotal role in characteristics of the splitting these energy levels, which can be categorized based on the irreducible representations of the S$_4$ point group. Thus, identifying the term value of Tm^{3+} ion and the corresponding irreducible representations of this point group is essential before we proceed with our discussion. To this end, we notice that the Tm^{3+} ion, characterized by 12 electrons in its f orbital, exhibits a total spin $S = 1$, total orbital angular momentum $L = 5$, and total angular momentum $4 \leqslant J \leqslant 6$, derived from the relation $|L - S| \leqslant J \leqslant |L + S|$. According to Hund's third rule for a given term (specified by particular values of L and S), the level with the highest J value lies lowest in energy if the shell is more than half-filled. If the shell is less than half-filled, the level with the lowest J value lies lowest in energy. The electron configuration of neutral Thulium (Tm) is [Xe]4f^{13}6s^2. When it loses three electrons to become Tm^{3+}, these electrons are typically removed from the outermost shell first, so the ion's electron configuration becomes [Xe]4f^{12}. Thus, for Tm^{3+} ion, the shell is more than half-filled, leading to $J = L + S = 5 + 1 = 6$ for the ground state. Consequently, the term value for the ground state configuration is $^3H_6$, as presented in Table V in Ref. [36]. The energy levels are split by the S$_4$ symmetric CF, and each level is labeled by the irreducible representations of the S$_4$ point group, denoted as Γ_i. The classifications and corresponding energy level details are thoroughly presented in Table V of Ref. [36]. For $J = 6$, there are 13 states, viz. $2J + 1 = 2 \times 6 + 1 = 13$. However, in agreement with experimental observations, our results show the presence of three doublet states. Therefore these 3 states should be subtracted from the original count of 13 states, resulting in a

TABLE IV. Number of $^3H_6$ multiplet split states for Tm^{3+} ions in $LiTmF_4$, denoted as i, and their degeneracy singlet and doublet states, denoted as "States." Calculated parallel and normal components of the dimensionless $\boldsymbol{g}_i$ tensor ($g_{i\perp}$ and $g_{i\parallel}$) and Van Vleck (vV) susceptibility ($\chi^{vV}_{i\perp}$ and $\chi^{vV}_{i\parallel}$, in units of $\mu_B T^{-1}$) are presented at zero temperature. These values were derived using DFT+CFT+Δ+Zeem.+Reg. with a hybridization parameter of $\Delta = -0.5$ Ry and the SPM+CFT+Zeem.+Reg. methods. For comparison we list also experimental $\boldsymbol{g}_i$ tensor values for Tm^{3+} ions in $LiYF_4$:Tm^{3+} [31].

Method		DFT+CFT+Δ+Zeem.+Reg.				SPM+CFT+Zeem.+Reg.					Emp.	
i	States	$g_{i\perp}$	$g_{i\parallel}$	$\chi^{vV}_{i\perp}$	$\chi^{vV}_{i\parallel}$	States	$g_{i\perp}$	$g_{i\parallel}$	$\chi^{vV}_{i\perp}$	$\chi^{vV}_{i\parallel}$	States	$g_{i\parallel}$
1	singlet	0.001	0.000	0.5573	0.0195	singlet	0.000	0.000	0.3367	0.0246	singlet	
2	doublet	0.000	0.624	−0.0377	0.0127	doublet	0.000	0.609	−0.0239	0.0124	doublet	0.494
3	singlet	0.000	0.000	−0.4518	0.0114	singlet	0.000	0.000	−0.253	0.0099	singlet	
4	singlet	0.000	0.003	0.0758	0.7513	singlet	0.000	0.000	0.0569	0.3241	singlet	
5	singlet	0.000	0.003	0.0523	−0.6563	singlet	0.000	0.000	0.0627	−0.2646	singlet	
6	singlet	0.000	0.001	0.3172	0.3341	singlet	0.000	0.001	0.1647	0.3834	singlet	
7	doublet	0.001	1.368	0.3014	0.6022	doublet	0.000	4.821	0.2674	0.2302	doublet	10.98
8	doublet	0.017	6.233	0.5438	−0.6148	singlet	0.003	0.001	−0.5884	−0.3933	doublet	3.506
9	singlet	0.212	0.000	−1.6164	0.0200	doublet	0.000	2.764	0.0196	0.2425	singlet	
10	singlet	0.001	0.000	−0.5491	−0.1144	singlet	0.000	0.000	−0.3042	−0.0840	singlet	
Ref.					This study							[31]

total of 10 states, viz. $13 - 3 = 10$ states, as tabulated in Tables II and IV.

In Table II, under the "DFT + CFT + Δ + Zeem. + Reg." column, we have presented the energies for the $^3H_6$ multiplet of Tm^{3+} ions in $LiTmF_4$, denoted as $\varepsilon_i(0)$. These values represent the energy levels resulting from CF splitting in the absence of an external magnetic field. We derived these values by performing quadratic regression on the energy levels computed in the presence of a magnetic field, as discussed in Sec. IV B. Specifically, the $\varepsilon_i(0)$ values were extrapolated from the $\varepsilon_i(\boldsymbol{B})$ relationships at zero magnetic field, shown in Fig. 3. The energy at $\boldsymbol{B} = 0$ converges to the same value for each state in both the [001] and [100] directions, indicating that a single column for "DFT + CFT + Δ + Zeem. + Reg." results in the table suffices. This can be clearly observed by comparing the pairs of figures in Fig. 3, specifically (a$_i$) with the corresponding c$_i$ for each i ranging from 1 to 10.

Conversely, the "DFT + CFT + Δ" column in Table II displays our previously calculated energies for the same multiplet, as detailed in [36]. These values, also arising from CF effects in zero magnetic field, were obtained directly from our DFT + CFT + Δ calculations, where the magnetic field ($\boldsymbol{B}$) was set to zero from the outset. The graphical representation of energy level splitting in $LiTmF_4$ is illustrated in Fig. 7(c) of Ref. [36]. The comparison between the "DFT + CFT + Δ + Zeem. + Reg." and "DFT + CFT + Δ" data, which incorporate a hybridization parameter of $\Delta = -0.5$ Ry, demonstrates excellent agreement. The close match between these two independent theoretical approaches reinforces the credibility of the energy levels determined for the Tm^{3+} ion in this compound. This congruence not only validates our regression-based approach but also strengthens the theoretical basis of our study, ensuring the reliability and accuracy of our model in capturing the intrinsic electronic structure of the $LiTmF_4$ compound under different conditions.

Furthermore, the energy eigenvalues obtained from the SPM provide an additional pathway for theoretical validation. While the SPM results generally indicate slightly higher energy levels compared to the *ab initio* and regres-

sion calculations, the differences are not substantial. This consistency across different computational approaches, each with its unique considerations, serves to reinforce the overall reliability of our theoretical models. The close agreement between the SPM and *ab initio* results, in particular, underscores the robustness of our computational methods in capturing the energy landscape of Tm^{3+} ions in $LiTmF_4$. It highlights the value of using diverse theoretical frameworks to gain a well-rounded understanding of the material's electronic structure and its interactions with external factors.

Our theoretical findings are significantly bolstered when compared with experimental and empirical data. This alignment is particularly evident in the lower energy states, as seen in our comparisons with neutron spectroscopy measurements of $LiTmF_4$ [17], absorption spectra of Tm^{3+} in $LiTmF_4$ [35], and optical spectroscopy and theoretical studies of Tm^{3+} in $LiYF_4$:Tm^{3+} [31]. Our calculated multiplet energies, especially for the lower energy states like the 1st singlet and 2nd doublet, closely agree with these experimental values, thus confirming the accuracy of our computational approach in understanding the Tm^{3+} ion's electronic structure. While there are deviations in the calculated energies of these lower states compared to the experimental data, these discrepancies highlight the complexities inherent in capturing CF effects within theoretical models. The variability in agreement for the higher energy states may indicate their increased sensitivity to the specifics of theoretical modeling and experimental conditions.

The consistency in empirical and experimental data points with those obtained in our calculations underlines the effectiveness of empirical adjustments to the former data in bridging theoretical predictions with observations. This is especially relevant in areas where direct experimental measurements are challenging. The integration of the hybridization parameter in the *ab initio* calculations further enhances this accuracy, emphasizing the importance of detailed electronic interaction considerations in accurate modeling.

The data presented in Table II underscore the valuable role of diverse computational methods in understanding the

electronic properties of rare-earth doped materials. The close alignment of *ab initio* and regression methods with experimental results for lower energy states is particularly encouraging, indicating that these theoretical approaches can effectively capture the complex interactions governing the electronic structure of Tm^{3+} ions in $LiTmF_4$. The discrepancies observed, especially in the higher energy states and between the SPM and other methods, highlight the need for further research. These may include refining theoretical models, conducting more detailed experiments, and exploring the effects of various CFPs.

It is through this synthesis of theoretical rigor and experimental validation that the value of our *ab initio* results is truly manifested. The ability of these results to not only stand in agreement with experimental data but also to provide a predictive capability for understanding the electronic transitions in the absence of an external magnetic field is indispensable. Our findings reveal the potential of computational methods to unravel the complexities of lanthanide-doped crystal systems and thus contribute meaningfully to the field of solid-state physics.

D. Parallel and normal components of effective Zeeman g_i-tensor and VanVleck susceptibility χ_i tensor

In this section, we analyze the magnetic properties of Tm^{3+} ions in $LiTmF_4$ at zero temperature, whereas the magnetic properties at higher temperatures are analyzed in section IV E. This involves calculating both the parallel and normal components of the dimensionless g_i tensor, denoted as $g_{i\parallel}$ and $g_{i\perp}$, as well as the Van Vleck (vV) susceptibility tensor, symbolized as $\chi_{i\parallel}^{vV}$ and $\chi_{i\perp}^{vV}$ in the units of $\mu_B T^{-1}$, respectively. The results are derived from quadratic regression of energy levels under varying external magnetic fields using Eq. (12), as discussed in Sec. IV B.

The results tabulated in Table IV (see, sets "DFT + CFT + Δ + Zeem. + Reg." and "SPM + CFT + Zeem. + Reg.") offer insight into comprehensive view of the magnetic properties of Tm^{3+} ions in $LiTmF_4$. For both the g_i and χ_i tensors, we derived their normal (parallel) components by applying the external magnetic field along the [100] ([001]) direction. The derivation involved fitting the magnetic field's influence on the energy levels of Kramers states using Eq. (12), based on our prior DFT + CFT + Δ data with a hybridization parameter $\Delta = -0.5$ Ry [36] and our current SPM + CFT results.

By analyzing these components at zero temperature, we aim to unravel the nuanced interplay between the magnetic field and the intrinsic magnetic properties of the compound. This exploration is pivotal in advancing our understanding of the material's fundamental magnetic characteristics and in laying the groundwork for potential applications in low-temperature physics and magnetic technology.

Using Eq. (11), $g_{i\parallel}$ is calculated with $\boldsymbol{B}$ along the [001] axis, whereas $g_{i\perp}$ with $\boldsymbol{B}$ along the [100] axis, which for the studied crystal is equivalent to the [010] direction. Analysis of the results given in Table IV provides insights into the behavior of Tm^{3+} ions in $LiTmF_4$ under $\boldsymbol{B}$—field at zero temperature and the contributions from the doublet and singlet states.

In the case of doublet states, our findings are quite revealing. The parallel components of the g_i tensor exhibit nonzero values. This phenomenon indicates a substantial interaction between these states and the applied magnetic field, a pattern that we have catalogued in Table IV. This observation is not just a mere data point but aligns with our theoretical predictions about the Zeeman effect's influence on these degenerate states. It underscores the nuanced way in which doublet states react to external magnetic fields.

Conversely, the situation is markedly different for singlet states. Here, we observe that the components of the g_i tensor are almost negligible, a stark contrast to what is observed in doublet states. This observation, also documented in Table IV, is in harmony with our expectation for the nondegenerate singlet state and the analytic predictions provided by Eq. (13). It suggests that the energy of non-Kramers singlet states, as articulated in this equation, is influenced solely by the magnetic field vector and the susceptibility tensor, with no dependence on the g_i tensor. This is a critical distinction from the Kramers doublet states, where the energy, as elucidated in Eq. (12), is dependent not only on the magnetic field vector and the susceptibility tensor but also crucially on the g_i tensor. Such a contrast highlights the divergent responses of these electronic states under the influence of a magnetic field. The negligible g values observed in the singlet states validate the accuracy of our DFT + CFT + Δ results and the methodology employed. This is despite our use of the Kramers equation, Eq. (12), which involves the g_i tensor, instead of Eq. (13) applicable for the non-Kramers singlet states, which does not involve a g_i tensor.

Besides the successful observations discussed in the previous two paragraphs regarding the behaviors of parallel and perpendicular components of the g-factor for singlet and doublet states, which align with experimental data, there are some numerical limitations of the methods that need to be addressed and discussed. For instance, from Table IV, one notices that the g-factor, including both its parallel and perpendicular components, for the singlet states are almost vanishing, except for the state $i = 9$, which shows a small but nonzero magnitude using the DFT + CFT + Δ + Zeem. + Reg. method. Empirically, only the $g_{i\parallel}$ components of the doublet states are reported [31], since only these components are experimentally measured to be nonzero. That is, $g_{i\perp}$ for doublet states and both $g_{i\parallel}$ and $g_{i\perp}$ for singlet states are expected to be zero, as shown in Table IV. Therefore the latter observations are numerical artifacts and do not necessarily have a physical origin. Our analyses show that these numerical limitations originate from the following practical procedure. In principle, Eq. (12) is formulated for Kramers doublet states, while Eq. (13) is expressed for non-Kramers singlet states. The former Kramers equation includes three terms: a constant term, a linear term with respect to the magnetic field, and a quadratic term with respect to the magnetic field. In Eq. (12), the linear term contains the g_i tensor, while the quadratic term contains the χ_i tensor. The non-Kramers Eq. (13) has only two terms: a constant term and a quadratic term with respect to the magnetic field. In Eq. (13), the quadratic term also contains the χ_i tensor, whereas the linear term and, as a result, the g_i tensor, are not included. The absence of the linear term and thereby the g_i tensor in Eq. (13) leads to a vanishing g factor

for all the singlet states. This explains why the g factor is physically expected to be zero. The non-Kramers Eq. (13), due to the absence of the $\boldsymbol{g}_i$ tensor, cannot be used for the doublet state. However, Eq. (12), in addition to the Kramers doublet states, can be used for the non-Kramers singlet states, as well. Eq. (12), in addition to the linear term, involves both constant and quadratic terms, which are necessary for the study of singlet states. In fact, the Kramers equation is mathematically more general than the non-Kramers equation. Therefore, in practice, for both singlet and doublet states, the first and second methods applied utilize Eq. (12) due to its more general form, encompassing the constant term and both the linear and quadratic terms. Using Eq. (12) for singlet states is quite successful, because both the parallel and perpendicular components of the g factor, as the coefficients of the linear term in this equation, are almost vanishing, except for the case of state $i = 9$ with the DFT + CFT + Δ + Zeem. + Reg. method. This nonvanishing exceptional case originates numerically from fitting the data using the more general Eq. (12) for the non-Kramers singlet states. Obviously, if we used the non-Kramers Eq. (13) for fitting, we would find all the parallel and normal components of the g factor to be exactly zero for all singlet states, including the state $i = 9$, as there is no any $\boldsymbol{g}_i$ tensor in Eq. (13). This shows that the source of the nonzero value for the singlet state $i = 9$, as predicted by the DFT + CFT + Δ + Zeem. + Reg. method, originates just numerically. Although the g factor of the singlet state $i = 9$ is physically expected to be zero, it does not seriously affect the physical results due to its small value, so that our physical predictions remain consistent with the experimental data.

We have also found that in both doublet and singlet states, the normal and parallel components of the $\boldsymbol{\chi}_i$ tensor display nonzero values. These observations are not only consistent across both states but also align with the analytic predictions for non-Kramers doublet states [Eq. (13)] and Kramers singlet states [Eq. (12)], where the $\boldsymbol{\chi}_i$ tensor is explicitly presented.

This table extends our understanding of the $\boldsymbol{g}_i$ tensor components ($g_{i\perp}$ and $g_{i\parallel}$) and Van Vleck susceptibility ($\chi_{i\perp}^{vV}$ and $\chi_{i\parallel}^{vV}$) for the $^3H_6$ multiplet states of Tm^{3+} ions, as calculated using both DFT + CFT + Δ methods and the SPM + CF. Additionally, it compares these results with available experimental data for Tm^{3+} in $LiYF_4:Tm^{3+}$, offering a comprehensive perspective on the theoretical and empirical aspects of these magnetic properties.

Comparison of the theoretical results with available experimental data for Tm^{3+} in $LiYF_4:Tm^{3+}$, offers insight into its magnetic properties. Note that the distinction between the g factors for atoms and ions in solids arising from the crystal field effects is discussed in Sec. SIII in Ref. [40].

Moreover, we make a comparison between our theoretical findings and the available experimental $\boldsymbol{g}_i$ tensor values for Tm^{3+} ions in $LiYF_4:Tm^{3+}$, as reported in [31]. It is important to note, however, that the $LiYF_4:Tm^{3+}$ compound used in the experimental study is not identical to our $LiTmF_4$ compound, meaning that an exact match in the results is not anticipated due to the subtle differences between these compounds. While the "SPM + CFT + Zeem. + Reg." and "DFT + CFT + Δ + Zeem. + Reg." calculations show enhanced compatibility, suggesting the model's effectiveness in certain scenarios, there are some discrepancies between the

calculated $g_{i\parallel}$ values and the experimental data, especially for the second excited doublet state. These variations, however, should not be viewed as drawbacks. Instead, they highlight the complex nature of magnetic interactions in these materials and underscore the need for a nuanced understanding in their study. These occasional discrepancies between theory and experiment do not diminish the value of our results but may suggest refinements to improve either the computational models or experimental techniques. Thus such discrepancies could be seen as an impetus for further research.

The signs of the Van Vleck susceptibility, both positive and negative, see Table II, are indicative of the intricate behavior of singlet states under magnetic influence, as visualized in Fig. 3. This correlation between the susceptibility and the energy of the singlet and doublet states offers a deeper insight into the magnetic properties of Tm^{3+} ions in $LiYF_4:Tm^{3+}$, thus improving our understanding of these systems.

E. Temperature dependence of magnetic moment and susceptibility

In the preceding sections, we systematically extended our analysis from the exclusive consideration of crystalline fields in the absence of magnetic influences at zero temperature, incorporating the effects of magnetic fields through the application of Zeeman interaction. Here, we further generalize the latter extension to nonzero temperatures, applying Boltzmann statistics to account for thermal effects.

In this section, we further generalize the latter extension to nonzero temperatures, applying Boltzmann statistics to account for thermal effects. This enables exploring the temperature variations in the magnetization (see Fig. 4) and susceptibility (see Fig. 5), per Tm^{3+} ion of $LiTmF_4$ in the x and z directions when an external magnetic field of 0.1 T is aligned parallel to these respective directions.

Here, we utilize the computed parallel and normal components of the $\boldsymbol{g}_i$ tensor ($g_{i\perp}$ and $g_{i\parallel}$), magnetic moment ($M_\perp$ and $M_\parallel$), and Van Vleck (vV) susceptibility ($\chi_{i\perp}^{vV}$ and $\chi_{i\parallel}^{vV}$), as discussed in Sec. IV D, along with Eqs. (12), (14), (15), and (16), as discussed in Sec. II A.

The above methodological framework, which integrates DFT with CFT, and further includes corrections for Zeeman splitting and Boltzmann thermal distribution, is designated as DFT + CFT + Δ + Zeem. + Boltz., where Δ represents an adjustable parameter fine-tuned to closely align theoretical outcomes with experimental data. In this method, the CFPs were derived from diverse hybridization strengths between the $4f$ electrons and the $2p$ and $2s$ orbitals of the fluorine ligands using various values of the Δ parameters.

The results calculated using DFT + CFT + Δ + Zeem. + Boltz. with Δ equal: -0.3, -0.4, and -0.5, are shown in panel (a) of Figs. 4 and 5 for the x direction and in their panel (b) for the z direction. Considering a nonlinear logarithmic scale for the temperature axis in panels (a) and (b) of these figures, we include results obtained from SPM + CFT + Zeem. + Boltz., alongside experimental and empirical data from Ref. [16] for comparison. This presentation enables examination of magnetization and susceptibility variations, providing insights into the interplay between temperature, hybridization effects, and crystallographic orientation (see, subsequent sections). The
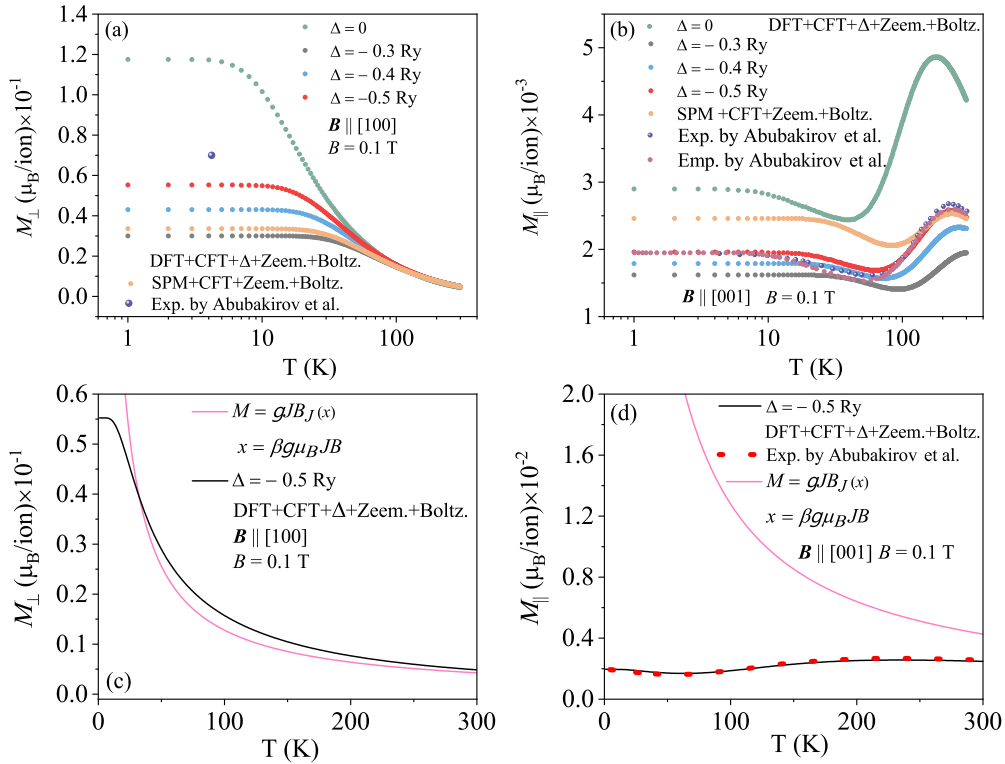
FIG. 4. Temperature-dependent magnetization of Tm^{3+} Ions in $LiTmF_4$ using the DFT + CFT + Δ + Zeem. + Boltz. *ab initio* scheme. (a) and (c) illustrate the magnetization as a function of temperature under an external magnetic field of 0.1 T along the [100] crystallographic axis, while (b) and (d) display the magnetization under the **B** = 0.1 T but applied along the [001] direction. The variation in magnetization is explored by considering different Δ parameters, indicative of varying degrees of hybridization in (a) and (b). Moreover, theoretical predictions are computed using Eq. (S16), see Sec. SIII in Ref. [40], with $g = 7/6$ and $J = 6$. The latter results are compared in (c) and (d) with our *ab initio* results calculated using optimized parameter $\Delta = -0.5$ Ry, as well as with the experimental data [16]. A nonlinear logarithmic scale is utilized on the temperature axis in (a) and (b) to enable a clear comparison with the experimental data.

inclusion of a logarithmic temperature scale in Figs. 4(a) and 4(b) enables to discern and compare the subtle nuances of magnetic behavior at lower temperatures, thus ensuring a thorough and targeted analysis.

To validate the quality of reproducing the expected asymptotic behaviors, we compare, in panels (c) and (d) of Figs. 4 and 5, our analytic predictions from Eq. (S16) with $g = 7/6$ and $J = 6$ (detailed in Ref. [40]), against our DFT + CFT + Δ + Zeem. + Boltz. results calculated using optimized parameter $\Delta = -0.5$ Ry.

1. $M_\perp(T)$ and $M_\parallel(T)$ at B = 0.1 T

Analysis of the normal component of magnetization $M_\perp$, shown in Fig. 4(a), reveals a notable discrepancy between theoretical predictions DFT + CFT + Δ + Zeem. + Boltz. without hybridization ($\Delta = 0$) and the experimental low-temperature data [16]. The fact that theoretical values of $M_\perp$ consistently surpass the experimental ones for $LiTmF_4$ can be resolved by taking into account hybridization effects. This highlights crucial role of hybridization in accurately representing the magnetization process at the quantum scale.

Incrementally introducing hybridization parameters, with Δ ranging from -0.3 to -0.5 Ry, results in a progressive alignment with experimental observations. The optimal

agreement is achieved at the highest considered hybridization level ($\Delta = -0.5$ Ry).

In the low-temperature domain, the SPM + CFT + Zeem. + Boltz. model generates magnetization curves for $M_\perp$ that fall in an intermediate position compared to the results from the DFT + CFT + Δ + Zeem. + Boltz. model, across Δ values ranging from -0.3 to 0.4 Ry. This model exhibits a closer alignment with the predictions at $\Delta = -0.3$ Ry, underscoring the nuanced role of hybridization effects in determining $M_\perp$ at quantum scales.

Our findings indicate an absence of notable temperature dependence in ion magnetization below roughly 10 K for the DFT + CFT + Δ + Zeem. + Boltz. approach with $\Delta = -0.5$ Ry, and below approximately 11 K for the SPM + CFT + Zeem. + Boltz. model. This behavior is consistent with the characteristics of Van Vleck paramagnets, which is attributed to quantum mechanical mixing of quantum states rather than thermal population effects (see, Sec. SIV in Ref. [40]). These findings are corroborated by the temperature independent experimental magnetization below 8 K [16], thus indicating the Van Vleck paramagnetic contribution in our sample.

At high temperatures, theoretical predictions SPM + CFT + Zeem. + Boltz. and DFT + CFT + Δ + Zeem. + Boltz. across all Δ values converge, thus reflecting the relationship between temperature, hybridization, and
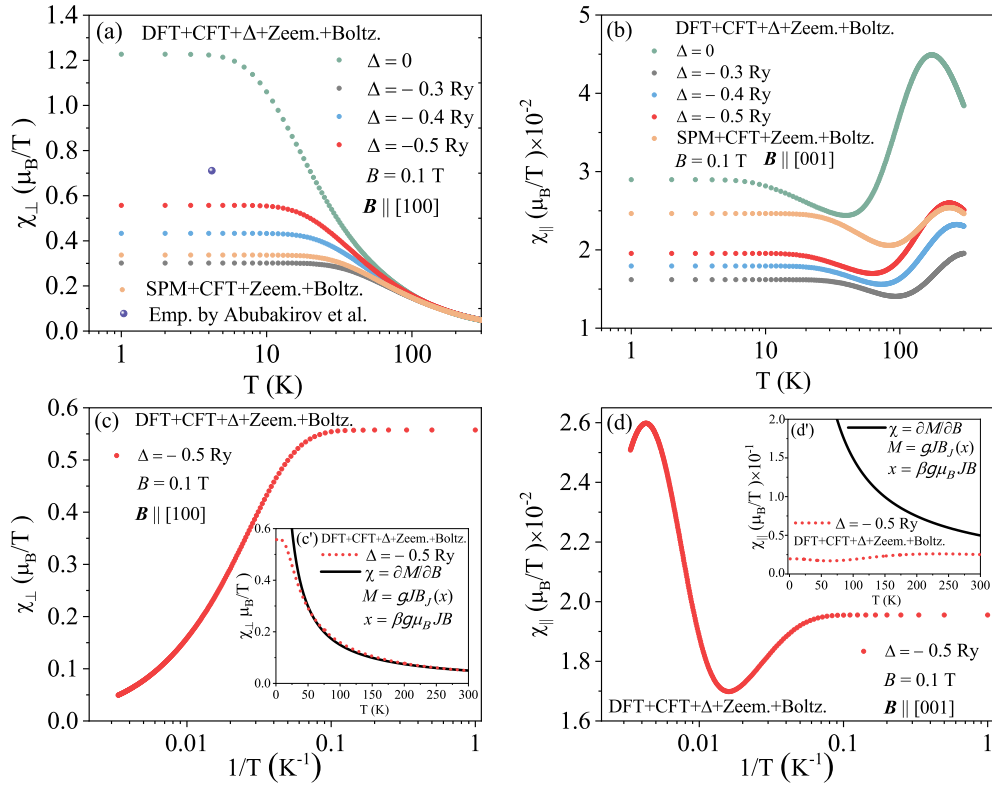
FIG. 5. Temperature-dependent magnetic susceptibility of Tm^{3+} in $LiTmF_4$: [(a) and (b)] magnetic susceptibility (χ) of Tm^{3+} ions in $LiTmF_4$ plotted against temperature and [(c) and (d)] against inverse temperature. The external magnetic field of 0.1 T was applied along the [100] axis for (a), (c), and (c′) and the [001] axis for (b), (d), and (d′). Variations in the Δ parameter correlate with increasing hybridization levels. In (a) and (b), the data are obtained from two complementary approaches: (1) SPM + CFT + Zeem. + Boltz., and (2) DFT + CFT + Δ + Zeem. + Boltz. with various Δ parameters. In (c) and (d), the results obtained from DFT + CFT + Δ + Zeem. + Boltz. with the optimized $\Delta = -0.5$ Ry are plotted as functions of inverse temperature to examine the Curie behavior. In insets (c′) and (d′), the data derived from a model of noninteracting, localized R^{3+} magnetic ions in a magnetic field (indicated by black curve) are compared with the results obtained from DFT + CFT + Δ + Zeem. + Boltz. with the optimized $\Delta = -0.5$ Ry, as using a model Hamiltonian accounting for magnetic ion interactions within the crystal lattice (indicated by red stars). In (a)–(d), a nonlinear logarithmic scale is used to accentuate low-temperature behaviors.

magnetization behavior. This convergence, particularly noticeable as temperatures significantly increase, aligns with the anticipated high-temperature behavior where magnetization approaches zero. Several factors may contribute to the decrease in $M_\perp$ for individual Tm atoms in $LiTmF_4$. Despite Van Vleck paramagnetism's general temperature-independence, at high temperatures, thermal energy may populate higher energy states not involved in the Van Vleck process, reducing the effective magnetic moment per Tm atom. Additionally, thermal agitation can disrupt the Tm atoms' local environments, altering their electronic energy levels and magnetic moments. Although phonon temperature effects are not explicitly included in the current calculations, we predict that phonon interactions within the crystal lattice at elevated temperatures may affect the Tm^{3+} ions' energy levels, thus affecting magnetization. Furthermore, the assumption of independent Tm atom behavior may be invalid at the higher thermal energy, as interactions among Tm and Li atoms—and their collective behavior—become significant. Therefore, while the overall magnetization of $LiTmF_4$ aligns with Van Vleck paramagnetic characteristics, an individual Tm atom's magnetization is expected to decline

at high temperatures due to these factors. This decline reflects the intricate thermal dynamics within the Tm atoms' electronic states in this unique Van Vleck paramagnetic system.

In essence, our observation from Fig. 4(a) reveals the delicate balance between hybridization, temperature, and quantum mechanical effects on the magnetization of $LiTmF_4$. The findings highlight the importance of considering hybridization and quantum mechanical mixing of states for accurate theoretical predictions, especially in the context of Van Vleck paramagnetism and its manifestations in experimental magnetization data.

In Fig. 4(b), the magnetization of Tm^{3+} ions, $M_\parallel$, under a magnetic field applied along the [001] direction, is markedly lower than in Fig. 2(a), where the field is along the [100] direction, $M_\perp$, showcasing the anisotropic magnetic response of $LiTmF_4$. Quantitatively, $M_\perp$ surpasses $M_\parallel$ by approximately one to two orders of magnitude across the temperature spectrum. This anisotropy highlights the significant role of crystallographic direction in magnetic behavior, as confirmed by experimental data [16] and validated by our theoretical calculations.

Without hybridization ($\Delta = 0$), theoretical outcomes from DFT + CFT + Δ + Zeem. + Boltz. approach like SPM + CFT + Zeem. + Boltz. model exceed empirical observations, while the inclusion of hybridization ($\Delta = -0.3$ Ry) produces estimates below the experimental data, emphasizing hybridization's pivotal impact. However, for $\Delta = -0.4$ and -0.5 Ry, at certain temperatures, the results are in close agreement with experimental observations. Particularly, the theoretical prediction of $M_\parallel$ using the DFT + CFT + Δ + Zeem. + Boltz. approach with $\Delta = -0.4$ Ry closely matches experimental findings between 20 and 70 K, thus marking a departure from its own trend of underestimation observed at most other temperatures within the 0 to 300 K range. Throughout the latter temperature range, the theoretical prediction of $M_\parallel$ using the DFT + CFT + Δ + Zeem. + Boltz. approach with $\Delta = -0.5$ Ry demonstrates a variable relationship with experimental data: it closely matches experimental findings between zero and 10 K; it is slightly higher in specific segments, accurately align around 250 K, yet very slightly undershoots in others. These observations show a specific temperature-dependent hybridization effect on the magnetic properties of Tm^{3+} ions in $LiTmF_4$, emphasizing the temperature sensitive nature of hybridization effects across the wide temperature range.

Based on the above analysis of Figs. 4(a) and 4(b), we deduce that DFT + CFT + Δ + Zeem. + Boltz. with $\Delta = -0.5$ Ry yields results that are more consistent with the experimental observations across a broader range of temperatures compared to $\Delta = -0.4$ Ry. While $\Delta = -0.4$ Ry is capable of accurately predicting some segments of the parallel component only, $\Delta = -0.5$ Ry is selected as the optimized value for the Δ parameter. This is because it not only more effectively captures the experimental $M_\perp$ but also aligns better with the experimental and empirical $M_\parallel$ over a wider temperature spectrum. Importantly, in our previous work [36], which examined other physical quantities and the density of states in the absence of a magnetic field at zero temperature, we identified -0.5 Ry as the optimized Δ parameter, as well. Now, extending this analysis to magnetization in two orthogonal directions relative to the external magnetic field over wide temperature range, we reaffirm -0.5 Ry as the optimized Δ value. This consistent finding across different studies significantly boosts our confidence in the results.

In Fig. 4(c), we evaluate the performance of the DFT + CFT + Δ + Zeem. + Boltz. approach, utilizing the optimized parameter $\Delta = -0.5$, in matching our analytic predictions formulated by Eq. (S16) with $g = 7/6$ and $J = 6$, as elaborated in Sec. SIII in Ref. [40]. This evaluation reveals that from approximately 40 to 300 K, the $M_\perp$ values predicted by the DFT + CFT + Δ + Zeem. + Boltz. model with $\Delta = -0.5$ align with the analytic predictions derived from Eq. (S16) with $g = 7/6$ and $J = 6$. This agreement implies that applying a magnetic field in the [100] direction does not significantly affect the magnetic behavior of R^{3+} ions within the above temperature range. This inference is drawn from the fact that Eq. (S16) was derived from studying an ensemble of noninteracting, localized R^{3+} magnetic ions under an external magnetic field, without the influence of a CF, utilizing a statistical mechanics approach within the context of a canonical ensemble framework. In contrast, our DFT +

CFT + Δ + Zeem. + Boltz. approach is designed to study the system when interactions are present.

Figure 4(d) indicates that the conclusions regarding the $M_\perp$ component, as inferred from Fig. 4(c), do not apply to the $M_\parallel$ component. Specifically, in the [0, 150 K] temperature interval, the curve representing noninteracting ions—obtained from Eq. (S16) with $g = 7/6$ and $J = 6$—significantly diverges from that representing interacting ions computed by the DFT + CFT + Δ + Zeem. + Boltz. scheme with the optimized parameter $\Delta = -0.5$. Despite the discrepancy between the results obtained for noninteracting and interacting ions, the values of $M_\parallel$ computed by the DFT + CFT + Δ + Zeem. + Boltz. scheme with $\Delta = -0.5$ for interacting ions demonstrate excellent agreement with the experimental data [16]. It is worth noting that the curves obtained for noninteracting and interacting ions as well as experimental ones, start to converge at higher temperatures. The analysis of Figs. 4(c) and 4(d) reveals that the behavior of magnetization significantly varies with the direction of the applied magnetic field, further indicating a distinct magnetic anisotropy.

2. $\chi_\perp(T)$ and $\chi_\parallel(T)$ at $B = 0.1$ T

In the presence of a magnetic field strength of $B = 0.1$ T, our results show that the normal and parallel components of the magnetic susceptibility of the Tm^{3+} ion in $LiTmF_4$ exhibit temperature-dependent behaviors that are analogous to those of the magnetic moment. This analogy in temperature-dependent behavior between susceptibility and magnetic moment is highlighted by direct comparisons: Fig. 5(a) compared with Fig. 4(a) shows this for the normal components, and Fig. 5(b) alongside with Fig. 4(b) demonstrates it for the parallel components.

Given the observed similarity, we infer that the magnetic moments are approximately linear functions of the magnetic field strength in the vicinity of 0.1 T. This inference is supported by the fact that magnetic susceptibilities are calculated from the derivative of the magnetic moments with respect to the magnetic field strength, as outlined in Eq. (16). Consequently, by assuming a linear relationship between magnetization and the magnetic field, taking the derivative of magnetization with respect to the magnetic field simplifies to dividing the magnetization by the field.

We verified the validity of this inference using experimental data. To accomplish this, we extracted the experimental magnetization data measured across various magnetic fields from Ref. [16], as presented in the Fig. 6, and applied a third-order polynomial fit to them. This experimental analysis, depicted in Fig. 6, not only supports our initial inference about the linear behavior of magnetic moments in relation to the magnetic field strength but also provides a better understanding of the magnetization dynamics under varying magnetic fields.

The subtle variances in magnetization behavior compared to magnetic susceptibility, as illustrated in the Figs. 5 and 4(a), can be also elucidated by the equation derived from the fitting process. The polynomial fit to the experimental data, as indicated in Fig. 6, reveals that magnetization's response to the magnetic field exhibits nonlinear behavior in specific regions. In such scenarios, the simplified approach of calculating magnetic susceptibility by dividing magnetization by the
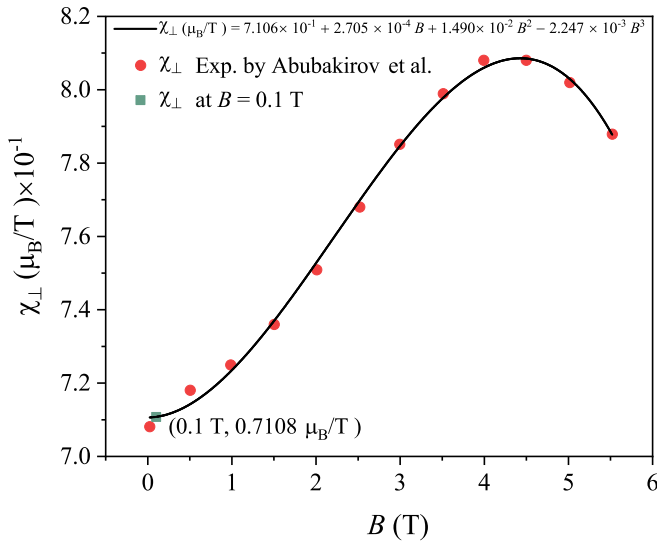
FIG. 6. Dependence of perpendicular susceptibility on magnetic field for Tm^{3+} ions in $LiTmF_4$ at 4.2 K, based on experimental data from Ref. [16]. The datum point at 0.1 T was derived by fitting the experimental data to correspond to 0.711 μ_B/T.

magnetic field becomes inadequate. Instead, a direct differentiation of magnetization with respect to the magnetic field is required to accurately determine magnetic susceptibility, as performed in this work.

Highlighting the susceptibility of $LiTmF_4$, our findings pivot around the significant influence of a narrow energy gap on its paramagnetic properties, particularly in the context of Van Vleck paramagnetism. This focus stems from the behavior of magnetic moments at low temperatures, as illustrated in Fig. 4(a), laying the groundwork for comprehending the patterns of susceptibility. Specifically, the energy gap of 5.08 meV (40.98 cm^{-1}) between the Tm^{3+} ion's singlet ground state and the first excited doublet, Γ_{34}^1, as tabulated in Table II, is paramount to the enhanced susceptibility observed in orientations perpendicular to the [001] axis. This calculated gap's proximity to the experimental value of 30 cm^{-1}, reported in Ref. [16], not only corroborates the high susceptibility characteristic of $LiTmF_4$ but also secures its classification as a Van Vleck paramagnet. The susceptibility's direct correlation to this energy gap, meticulously outlined in Eq. (S19) in Ref. [40], cements the linkage between the material's specific low-temperature magnetic behavior and its distinct susceptibility profile. This ensures a focused narrative that accentuates the susceptibility aspect while integrating all relevant values, citations, and figures.

To examine the Curie behavior across inverse temperatures, we analyze both the normal (perpendicular) and parallel components of the magnetic susceptibility of the Tm^{3+} ion in $LiTmF_4$, presented on a nonlinear logarithmic scale in Figs. 5(c) and 5(d), respectively. These observations highlight the Curie behaviors at distinct temperature ranges, reflecting the characteristic changes in magnetic susceptibility in this material.

Specifically, Fig. 5(c) reveals that the perpendicular susceptibility component, $\chi_{i\perp}$, displays Curie behavior below approximately 17 K. In contrast, the parallel component, $\chi_{i\parallel}$,

depicted in Fig. 5(d), manifests this behavior at temperatures above approximately 250 K.

Additionally, in Figs. 5(c′) and 5(d′), we compare the susceptibility per ion, calculated using Eq. (S16) with parameters $g = 7/6$ and $J = 6$, against predictions from the combined DFT + CFT + Δ + Zeem. + Boltz. model, where $\Delta = -0.5$. This comparison enables to assess the accuracy of our susceptibility calculations in capturing the material's magnetic behavior, providing insights into the efficacy of theoretical models in effectively capturing the interactions in $LiTmF_4$.

In this context, we scrutinized two contrasting theoretical frameworks: one depicting a noninteracting assembly of localized R^{3+} magnetic ions within a magnetic field, and another accounting for inter-ion interactions within the crystal structure. For details of the in-depth exploration of the methodologies employed and the results derived from this comparative analysis, see Ref. [40].

In our analysis, Figs. 5(c′) and 5(d′), alongside Figs. 4(c) and 4(d), demonstrate a critical observation: the convergence of susceptibility values from two theoretical models as temperature increases. This convergence underscores a key insight, namely, that the intermolecular interactions within the crystal diminish in significance at elevated temperatures. Consequently, the magnetic susceptibility behavior aligns more closely with that expected from a theoretical model of noninteracting magnetic ions. This observation directly suggests that at higher thermal energies, the magnetic behavior of $LiTmF_4$ approximates the idealized model of noninteracting ions, thus simplifying the complexity of intermolecular forces at play. Such findings not only highlight the nuanced temperature dependence of magnetic susceptibility but also clarify the conditions under which $LiTmF_4$'s susceptibility can be approximated by simpler theoretical models, offering valuable insights into the material's fundamental magnetic characteristics.

V. SUMMARY, CONCLUSIONS, AND OUTLOOK

We conducted a theoretical analysis of the crystal field (CF) splittings of the $^3H_6$ ground multiplet levels for Tm^{3+} ions in $LiTmF_4$ to examine its magnetic properties. This analysis involves the CF Hamiltonian, $\hat{H}_{CF}$, and the Zeeman interaction. The Tm^{3+} ions in $LiTmF_4$ have an S_4 site symmetry, leading to seven independent CF parameters (CFPs), which are in our CF approach. However, optical spectra fitting often employ only 6 (R-approach) or 5 (A-approach) CFPs due to computational convenience. The R-approach simplifies one pair of rank $k = 4$ and 6 CFPs into a single parameter by rotating $\hat{H}_{CF}$ around the z axis, aligned with the S_4 axis. Conversely, the A-approach approximates S_4 site symmetry to a higher D_{2d} symmetry. Nonetheless, neither the R-approach nor the A-approach fully suits the magnetic property studies.

In our study, we adopt a comprehensive DFT + CFT + Δ/SPM + CFT twofold approach, utilizing all seven CFPs previously computed via DFT and *ab initio* methods [36]. This allows us to accurately calculate the CF splitting of Tm^{3+} ions in $LiTmF_4$. The observed behavior of the first $^3H_6$ doublet level splitting under an external magnetic field aligns with our expectations and previous findings [73].

To rigorously evaluate the accuracy and reliability of the CFPs calculated in our prior work [36], we undertook a detailed analysis applying Noether's theorem [33] within the framework of CFT [34]. This analysis enabled us to scrutinize the conserved quantities (CQs) for both our own CFPs datasets and those reported in previous studies that used semiempirical methods [16,35]. As detailed in Sec. II B, our examination of CQs—crucial for understanding the algebraic symmetry properties of the S_4 symmetry CF Hamiltonian— allows for a comparative assessment of CFPs datasets from various sources. Our findings presented in Sec. IV A, indicate a significant level of consistency and compatibility across different CQs derived from these datasets. This notable correlation suggests that the CFPs sets we computed through two independent methods exhibit strong mutual coherence, thereby affirming their reliability for predicting the spectroscopic and magnetic properties of Tm^{3+} ions in $LiYF_4$.

The successful validation of the computed CFPs, based on scrutiny of CQs, has facilitated the accurate determination of the $^3H_6$ multiplet energies, alongside the g_i tensor and susceptibility components, all of which align closely with existing experimental data [16,31,33,35,37,67–70]. This achievement highlights the efficacy of our combined DFT + CFT + Δ/SPM + CFT approach in replicating experimental observations in $LiTmF_4$ under moderate external magnetic fields. Furthermore, our findings emphasize the critical need to consider the intricate low symmetry CF aspects occurring for the S_4 site symmetry, which arise from Noether's theorem [34], particularly when evaluating and comparing CFPs datasets from diverse origins and methodologies.

Our comprehensive methodology allows for a rigorous assessment of the accuracy of calculated CFPs sets and their substantive comparison with experimental counterparts. By laying down this robust framework, we've set the stage for future explorations and theoretical modeling of the optical and magnetic properties of rare-earth ions in materials containing R^{3+} ions at low symmetry sites. Adopting this approach holds the promise of unlocking detailed insights into various physical properties and phenomena governed by the CF, potentially enhancing our grasp of materials and broadening their application spectrum.

In our investigation into the magnetic properties of the Tm^{3+} ion in $LiTmF_4$, we focused on the energy levels computed in an external magnetic field ranging from 0 to 1 T to calculate both components of the g_i tensor ($g_{i\perp}$ and $g_{i\parallel}$) and the Van Vleck susceptibilities ($\chi_{i\perp}^{vV}$ and $\chi_{i\parallel}^{vV}$), employing quadratic regression. This involved formulating a Hamiltonian that includes the terms for free ion and CF interactions, as well as the (effective) Zeeman interaction. The comparison of our computed g_i tensor components with the experimental data for Tm^{3+} ion in $LiYF_4$:Tm [31] demonstrates reasonable agreement, reinforcing the accuracy of our approach. These findings are instrumental in further refining the Zeeman interaction parameters for effective spin Hamiltonian models in Electron Magnetic Resonance (EMR) analyses, thus contributing valuable insights for theoretical and experimental studies in the field.

Our results reveal that the absence of hybridization leads to an overestimation of the magnetization when compared to experimental observations. This overestimation is systematically reduced as the hybridization strength is increased, suggesting that the interaction between the $4f$ electrons of the Tm^{3+} ions and the surrounding environment plays a non-negligible role in the magnetic properties of $LiTmF_4$. The hybridization modulates the magnetic anisotropy, which is a critical factor for the correct description of magnetization at low temperatures.

Temperature has a pronounced effect on the magnetization, with a negligible temperature dependence observed below approximately 10–11 K for different values of the hybridization parameter Δ. This indicates that the thermal energy at low temperatures is insufficient to overcome the anisotropy energy barriers, resulting in a temperature-independent magnetization. However, as the temperature increases, thermal agitation begins to overcome these energy barriers, leading to a reduction in magnetization. The SPM + CFT + Zeem. + Boltz. scheme particularly underestimates the magnetization across most of the temperature range, emphasizing the need for a more accurate description that includes hybridization effects.

The significant difference between perpendicular and parallel magnetizations suggests strong magnetic anisotropy in $LiTmF_4$. This anisotropy is an intrinsic property of the Tm^{3+} ion's electronic structure, enhanced by the CF effects within the lattice. The perpendicular magnetization is notably higher than the parallel component, underscoring the importance of considering directional dependence in theoretical models.

A remarkable convergence of theoretical predictions with experimental data is observed at higher temperatures, signifying that the energy scales of the thermal and magnetic interactions become comparable. This convergence is indicative of the models capturing the essential physics of the system, despite the simplified assumptions that may be employed at lower temperatures.

The close agreement between the DFT + CFT + Δ + Zeem. + Boltz. calculations and experimental data, especially with the optimized Δ of -0.5 Ry, highlights the synergy between sophisticated *ab initio* methods and empirical observations. This agreement not only validates the theoretical framework but also provides a benchmark for further studies on similar systems.

Our research demonstrates that $LiTmF_4$'s magnetic susceptibility, in both normal and parallel orientations under a 0.1 T field, reflects the trends expected for temperature variations of magnetic moments. This aligns with a linear magnetic moment-field strength relationship at 0.1 T, supported by experimental evidence and polynomial analysis.

Notably, the material's susceptibility, enhanced by a narrow energy gap, confirms its Van Vleck paramagnetic characteristics, especially at low temperatures.

Comparative analyses underscore the reduced impact of intermolecular interactions at higher temperatures, aligning the behavior closer to a noninteracting magnetic ion model and providing deeper insights into the fundamental magnetic characteristics of $LiTmF_4$.

Furthermore, our study underscores the significance of hybridization in modeling the magnetization of rare-earth ion systems and demonstrates that the inclusion of hybridization parameters is essential for accurate predictions. The findings have broad implications for understanding the magnetic

properties of similar ionic systems, with potential applications in the design of magnetic materials and the exploration of quantum magnetic phenomena.

As a motivation for future research, investigating similar systems with different rare-earth ions stands as a promising avenue. Such explorations are anticipated to yield valuable insights into the universality of the observed behaviors, enriching our understanding of these systems.

Based on the overall the results of our study, it may be expected that our accurate determination of magnetic properties achieved by employing the combined DFT + CFT + Δ/SPM + CFT approach, which enables computationally

inexpensive calculations, may have useful applications also in quantum computing, magnetic resonance imaging (MRI), spintronics, and materials design.

[1] D. Billington, E. Riordan, M. Salman, D. Margineda, G. J. W. Gill, S. P. Cottrell, I. McKenzie, T. Lancaster, M. J. Graf, and S. R. Giblin, Radio-frequency manipulation of state populations in an entangled fluorine-muon-fluorine system, Phys. Rev. Lett. **129**, 077201 (2022).

[2] R. Komban, S. Spelthann, M. Steinke, D. Ristau, A. Ruehl, C. Gimmler, and H. Weller, Bulk-like emission in the visible spectrum of colloidal LiYF$_4$:Pr nanocrystals downsized to 10 nm, Nanoscale Adv. **4**, 2973 (2022).

[3] A. Beckert, M. Grimm, R. I. Hermans, J. R. Freeman, E. H. Linfield, A. G. Davies, M. Müller, H. Sigg, S. Gerber, G. Matmon, and G. Aeppli, Precise determination of the low-energy electronuclear hamiltonian of LiY$_{1-x}$Ho$_x$F$_4$, Phys. Rev. B **106**, 115119 (2022).

[4] T. Dollberg, J. C. Andresen, and M. Schechter, Effect of intrinsic quantum fluctuations on the phase diagram of anisotropic dipolar magnets, Phys. Rev. B **105**, L180413 (2022).

[5] M. Libersky, R. D. McKenzie, D. M. Silevitch, P. C. E. Stamp, and T. F. Rosenbaum, Direct observation of collective electronuclear modes about a quantum critical point, Phys. Rev. Lett. **127**, 207202 (2021).

[6] O. Solovyev and M. Miftakhova, Modeling and decoding of fine structure of electron-vibrational 5d - 4f luminescence spectra in LiRF$_4$:Ce^{3+} (R = Y, Lu) crystals, J. Lumin. **195**, 96 (2018).

[7] P. Fedorov, V. Semashko, and S. Korableva, Lithium rare-earth fluorides as photonic materials: 1. physicochemical characterization, Inorg. Mater. **58**, 223 (2022).

[8] C. Kraemer, N. Nikseresht, J. O. Piatek, N. Tsyrulin, B. D. Piazza, K. Kiefer, B. Klemke, T. F. Rosenbaum, G. Aeppli, C. Gannarelli, K. Prokes, A. Podlesnyak, T. Strässle, L. Keller, O. Zaharko, K. W. Krämer, and H. M. Rønnow, Dipolar antiferromagnetism and quantum criticality in LiErF$_4$, Science **336**, 1416 (2012).

[9] L. Gyongyosi and S. Imre, A survey on quantum computing technology, Comput. Sci. Rev. **31**, 51 (2019).

[10] M. T. Vlaardingerbroek and J. A. Boer, *Magnetic Resonance Imaging: Theory and Practice* (Springer, Berlin, Heidelberg, 2003).

[11] I. Žutić, J. Fabian, and S. Das Sarma, Spintronics: Fundamentals and applications, Rev. Mod. Phys. **76**, 323 (2004).

[12] I. R. Berkman, A. Lyasota, G. G. de Boo, J. G. Bartholomew, B. C. Johnson, J. C. McCallum, B.-B. Xu, S. Xie, R. L. Ahlefeldt, M. J. Sellars, C. Yin, and S. Rogge, Observing Er^{3+}

sites in Si with an *in situ* single-photon detector, Phys. Rev. Appl. **19**, 014037 (2023).

[13] A. M. Dibos, M. Raha, C. M. Phenicie, and J. D. Thompson, Atomic source of single photons in the telecom band, Phys. Rev. Lett. **120**, 243601 (2018).

[14] F. Auzel, S. Hubert, and D. Meichenin, Multifrequency roomtemperature continuous diode and Ar* laserpumped Er^{3+} laser emission between 2.66 and 2.85 μm, Appl. Phys. Lett. **54**, 681 (1989), .

[15] S. A. Al'tshuler, V. I. Krotov, and B. Z. Malkin, Giant magnetostriction in Van-Vleck paramagnetic LiTmF$_4$, Pis'ma Zh. Eksp. Teor. Fiz. **32**, 232 (1980) [JETP Lett **32**, 214 (1980)].

[16] D. I. Abubakirov, K. Matsumoto, H. Suzuki, and M. S. Tagirov, Anisotropic magnetization of the Van Vleck paramagnet LiTmF$_4$ at low temperatures and high magnetic fields, J. Phys.: Condens. Matter **20**, 395223 (2008).

[17] P. Babkevich, A. Finco, M. Jeong, B. Dalla Piazza, I. Kovacevic, G. Klughertz, K. W. Krämer, C. Kraemer, D. T. Adroja, E. Goremychkin, T. Unruh, T. Strässle, A. Di Lieto, J. Jensen, and H. M. Rønnow, Neutron spectroscopic study of crystal-field excitations and the effect of the crystal field on dipolar magnetism in LiRF$_4$ (R = Gd, Ho, Er, Tm, and Yb), Phys. Rev. B **92**, 144422 (2015).

[18] D. Bitko, T. F. Rosenbaum, and G. Aeppli, Quantum critical behavior for a model magnet, Phys. Rev. Lett. **77**, 940 (1996).

[19] F. Rucker and C. Pfleiderer, Compact susceptometer for studies under transverse field geometries at very low temperatures, Rev. Sci. Instrum. **90**, 073903 (2019), .

[20] P. Beauvillain, C. Chappert, J. Renard, J. Griffin, and I. Laursen, Critical behaviour of the uniaxial dipolar ferromagnets LiTbF$_4$ and LiHoF$_4$: Effect of dilution by Y^{3+}, J. Magn. Magn. Mater. **15-18**, 421 (1980).

[21] P. E. Hansen, T. Johansson, and R. Nevald, Magnetic properties of lithium rare-earth fluorides: Ferromagnetism in LiErF$_4$ and LiHoF$_4$ and crystal-field parameters at the rare-earth and Li sites, Phys. Rev. B **12**, 5315 (1975).

[22] L. Aminov, B. Malkin, and M. Teplov, Chapter 150 Magnetic properties of nonmetallic lanthanide compounds, in *Handbook on the Physics and Chemistry of Rare Earths*, Vol. 22 (Elsevier, Amsterdam, 1996), pp. 295–506.

[23] H. M. Rønnow, J. Jensen, R. Parthasarathy, G. Aeppli, T. F. Rosenbaum, D. F. McMorrow, and C. Kraemer, Magnetic excitations near the quantum phase transition in the Ising ferromagnet LiHoF$_4$, Phys. Rev. B **75**, 054426 (2007).

[24] A. Abragam and B. Bleaney, *Electron Paramagnetic Resonance of Transition Ions*, International Series of Monographs on Physics (Universities Press, Belfast, Northern Ireland, 1970).

[25] M. Yazdani-Kachoei, S. Rahimi, R. Ebrahimi-Jaberi, J. Nematollahi, and S. Jalali-Asadabadi, Thermoelectric properties plus phonon and de Haas–van Alphen frequencies, Sci. Rep. **12**, 663 (2022).

[26] R. Laskowski, G. K. H. Madsen, P. Blaha, and K. Schwarz, Magnetic structure and electric-field gradients of uranium dioxide: An *ab initio* study, Phys. Rev. B **69**, 140408(R) (2004).

[27] K. Haule, Exact double counting in combining the dynamical mean field theory and the density functional theory, Phys. Rev. Lett. **115**, 196403 (2015).

[28] P. Blaha, K. Schwarz, G. K. H. Madsen, D. Kvasnicka, J. Luitz, R. Laskowski, F. Tran, and L. D. Marks, *WIEN2k: An Augmented Plane Wave + Local Orbitals Program for Calculating Crystal Properties* (Technische Universität Wien, Vienna, Austria, 2024).

[29] M. Acikgoz, L. Mollabashi, S. Rahimi, S. Jalali-Asadabadi, and C. Rudowicz, DFT computations combined with semiempirical modeling of variations with temperature of spectroscopic and magnetic properties of Gd^{3+}-doped $PbTiO_3$, Phys. Chem. Chem. Phys. **25**, 3986 (2023).

[30] S. Salaün, M. T. Fornoni, A. Bulou, M. Rousseau, P. Simon, and J. Y. Gesland, Lattice dynamics of fluoride scheelites: I. Raman and infrared study of $LiYF_4$ and $LiLnF_4$ (Ln = Ho, Er, Tm and Yb), J. Phys.: Condens. Matter **9**, 6941 (1997).

[31] S. A. Klimin, D. S. Pytalev, M. N. Popova, B. Z. Malkin, M. V. Vanyunin, and S. L. Korableva, High-resolution optical spectroscopy of Tm^{3+} ions in $LiYF_4$: Crystal-field energies, hyperfine and deformation splittings, and the isotopic structure, Phys. Rev. B **81**, 045113 (2010).

[32] C. Rudowicz, Algebraic symmetry and determination of the "Imaginary" crystal-field parameters from optical spectra of f^n-ions. tetragonal symmetry, Chem. Phys. **97**, 43 (1985).

[33] C. Rudowicz and J. Qin, Trends in the crystal (ligand) field parameters and the associated conserved quantities for trivalent rare-earth ions at S_4 symmetry sites in $LiYF_4$, J. Alloys Compd. **385**, 238 (2004).

[34] C. Rudowicz and J. Qin, Noether's theorem and conserved quantities for the crystal- and ligand-field Hamiltonians invariant under continuous rotational symmetry, Phys. Rev. B **67**, 174420 (2003).

[35] H. P. Christensen, Spectroscopic analysis of $LiTmF_4$, Phys. Rev. B **19**, 6573 (1979).

[36] L. Mollabashi and S. Jalali-Asadabadi, Crystal fields of lithium rare-earth tetrafluorides and multiplet splitting of the +3 rare-earth ions, Phys. Rev. B **102**, 045120 (2020).

[37] H. P. Jenssen, A. Linz, R. P. Leavitt, C. A. Morrison, and D. E. Wortman, Analysis of the optical spectrum of Tm^{3+} in $LiYF_4$, Phys. Rev. B **11**, 92 (1975).

[38] V. Kumar, Vishwamittar, and K. Chandra, On the behaviour of the Tm^{3+} ion in YVO_4 $LiYF_4$, J. Phys. C **10**, 267 (1977).

[39] A. Klochkov, V. Naletov, I. Mukhamedshin, M. Tagirov, D. Tayurskii, and H. Suzuki, Magnetism and structural phase transitions in $LiTmF_4$ powders, J. Exp. Theor. Phys. Lett. **66**, 266 (1997).

[40] See Supplemental Material at http://link.aps.org/supplemental/10.1103/PhysRevB.110.054440 for providing detailed data on the crystalline environment of Tm^{3+} in $LiTmF_4$, including positional parameters, bond lengths, and angular coordinates of the ligands. It explores the interactions of noninteracting R^{3+} magnetic ions with an external magnetic field, using dipole interactions and the Langevin and Brillouin functions to illustrate ion behavior under various conditions. The Supplemental Material aims to validate the main paper's findings by comparing numerical results for the interacting system with analytical results for a noninteracting model, highlighting the importance of Van Vleck paramagnetism in understanding the magnetic properties of rare-earth ions, making the reading experience straightforward and engaging. Additionally, a list of abbreviations and their corresponding definitions is included to facilitate readability and provide a quick reference for readers.

[41] H. M. Crosswhite and H. Crosswhite, Parametric model for *f*-shell configurations. I. The effective-operator Hamiltonian, J. Opt. Soc. Am. B **1**, 246 (1984).

[42] W. T. Carnall, G. L. Goodman, K. Rajnak, and R. S. Rana, A systematic analysis of the spectra of the lanthanides doped into single crystal LaF_3, J. Chem. Phys. **90**, 3443 (1989).

[43] *Optical Spectra of Transparent Rare Earth Compounds*, edited by S. Hüfner (Academic Press, 1978), Chap. 2, pp. 14–37.

[44] C. Rudowicz and M. Karbowiak, Disentangling intricate web of interrelated notions at the interface between the *physical* (crystal field) Hamiltonians and the *effective* (spin) Hamiltonians, Coord. Chem. Rev. **287**, 28 (2015).

[45] C. Rudowicz, P. Gnutek, and M. Karbowiak, Forms of crystal field Hamiltonians–a critical review, Opt. Mater. (Amsterdam) **33**, 1557 (2011).

[46] J. Mulak and Z. Gajek, *The Effective Crystal Field Potential* (Elsevier, New York, 2000).

[47] D. J. Newman and B. Ng (eds.), *Crystal Field Handbook* (Cambridge University Press, Cambridge, 2000).

[48] G. Liu and B. Jacquier (eds.), *Spectroscopic Properties of Rare Earths in Optical Materials* (Tsinghua University Press/Springer, Berlin, 2005).

[49] B. G. Wybourne and L. Smentek, *Optical Spectroscopy of Lanthanides: Magnetic and Hyperfine Interactions* (CRC Press, Taylor & Francis Group, Boca Raton, 2007).

[50] B. Wybourne, *Spectroscopic Properties of Rare Earths* (Inter-science Publishers, New York, 1965).

[51] L. F. Chibotaru, A. Ceulemans, and H. Bolvin, Unique definition of the Zeeman-splitting g tensor of a Kramers doublet, Phys. Rev. Lett. **101**, 033003 (2008).

[52] P. Novák, V. Nekvasil, and K. Knížek, Crystal field and magnetism with Wannier functions: Orthorhombic rare-earth manganites, J. Magn. Magn. Mater. **358-359**, 228 (2014).

[53] C. Rudowicz and J. Qin, Can the low symmetry crystal (ligand) field parameters be considered compatible and reliable? J. Lumin. **110**, 39 (2004).

[54] D. Newman and B. Ng, The superposition model of crystal fields, Rep. Prog. Phys. **52**, 699 (1989).

[55] C. Rudowicz, P. Gnutek, and M. Açikgöz, Superposition model in electron magnetic resonance spectroscopy – a primer for experimentalists with illustrative applications and literature database, Appl. Spectrosc. Rev. **54**, 673 (2019) .

[56] Y. Wan-Lun and Z. Min-Guang, Spin-Hamiltonian parameters of ^{6}state ions, Phys. Rev. B **37**, 9254 (1988).

[57] Z.-Y. Yang, C. Rudowicz, and Y.-Y. Yeung, Microscopic spin-hamiltonian parameters and crystal field energy levels for the low C_3 symmetry Ni^{2+} centre in $LiNbO_3$ crystals, Phys. B: Condens. Matter **348**, 151 (2004).

[58] J. P. Perdew and A. Zunger, Self-interaction correction to density-functional approximations for many-electron systems, Phys. Rev. B **23**, 5048 (1981).

[59] S. J. Asadabadi, S. Cottenier, H. Akbarzadeh, R. Saki, and M. Rots, Valency of rare earths in RIn$_3$ and RSn$_3$: *ab initio* analysis of electric-field gradients, Phys. Rev. B **66**, 195103 (2002).

[60] S. Asadabadi and H. Akbarzadeh, Density functional approach to study structural properties and electric field gradients in rare earth materials, Phys. B: Condens. Matter **349**, 76 (2004).

[61] S. Jalali Asadabadi, Electronic structure and electric-field gradient analysis in CeIn$_3$, Phys. Rev. B **75**, 205130 (2007).

[62] P. Novák, K. Knížek, and J. Kuneš, Crystal field parameters with Wannier functions: Application to rare-earth aluminates, Phys. Rev. B **87**, 205139 (2013).

[63] A. A. Mostofi, J. R. Yates, G. Pizzi, Y.-S. Lee, I. Souza, D. Vanderbilt, and N. Marzari, An updated version of wannier90: A tool for obtaining maximally-localised Wannier functions, Comput. Phys. Commun. **185**, 2309 (2014).

[64] H. J. Monkhorst and J. D. Pack, Special points for Brillouin-zone integrations, Phys. Rev. B **13**, 5188 (1976).

[65] P. Novák, K. Knížek, M. Maryško, Z. Jirák, and J. Kuneš, Crystal field and magnetism of Pr^{3+} and Nd^{3+} ions in orthorhombic perovskites, J. Phys.: Condens. Matter **25**, 446001 (2013).

[66] S. Edvardsson and D. Åberg, An atomic program for energy levels of equivalent electrons: lanthanides and actinides, Comput. Phys. Commun. **133**, 396 (2001).

[67] C. K. Jayasankar, M. F. Reid, and F. S. Richardson, Comparative crystal-field analyses of $4f^N$n energy levels in $LiYF_4$:Ln^{3+} systems, Phys. Status Solidi B **155**, 559 (1989).

[68] C. Görller-Walrand and K. Binnemans, Optical spectroscopy and electronic structure of rare-earth ions in crystals, in *Handbook on the Physics and Chemistry of Rare Earth*, edited by K. Gschneidner, Jr. and L. Eyring (North-Holland, Amsterdam, 1996), Vol. 23, p. 121.

[69] X. Chen and Z. Luo, Crystal-field analysis of the spectroscopic characteristics and magnetic properties of Tm^{3+} in $LiYF_4$ crystal, J. Phys.: Condens. Matter **9**, 4197 (1997).

[70] J. Cheng, J. Wen, Y. Chen, M. Yin, and C. Duan, Crystal-field analyses for trivalent lanthanide ions in $LiYF_4$, J. Rare Earths **34**, 1048 (2016).

[71] C. Rudowicz, Transformation relations for the conventional $O_k{}^q$ and normalised $O'_k{}^q$ Stevens operator equivalents with $k = 1$ to 6 and $-k \leqslant q \leqslant k$, J. Phys. C **18**, 1415 (1985).

[72] K. Knížek, Z. Jirák, P. Novák, and C. de la Cruz, Non-collinear magnetic structures of $TbCoO_3$ and $DyCoO_3$, Solid State Sci. **28**, 26 (2014).

[73] R. Y. Abdulsabirov, A. A. Kazantsev, S. L. Korableva, B. Z. Malkin, S. I. Nikitin, A. L. Stolov, M. S. Tagirov, D. A. Tayurskii, and J. van Tol, Magnetic field effects in optical and far IR spectra of $LiTmF_4$ crystals, in *XI Feofilov Symposium on Spectroscopy of Crystals Activated by Rare-Earth and Transition Metal Ions, Kazan, Russian Federation*, edited by A. A. Kaplyanskii, B. Z. Malkin, and S. I. Nikitin, International Society for Optics and Photonics, Vol. 4766 (SPIE, 2002), pp. 59–64.

[74] I. Romanova, B. Malkin, and M. Tagirov, Multipole interactions in a $LiTmF_4$ single crystal, Opt. Spectrosc. **116**, 897 (2014).